

Faculty of Medicine, Master thesis in Pharmacy, June 2016

Maria Garli Hegvik

Quantitative analysis of binding and  
internalization of  $\alpha_v\beta_3$  integrin-targeted  
nanoemulsions by human endothelial cells  
- *in vitro*



Norwegian University of  
Science and Technology



# Contents

<b>1</b>	<b>Introduction.....</b>	<b>3</b>
<b>2</b>	<b>Theory.....</b>	<b>4</b>
2.1	Hallmarks of cancer.....	4
2.1.1	Targeting angiogenesis.....	5
2.2	Integrins.....	6
2.2.1	$\alpha_v\beta_3$ -integrin.....	8
2.3	Nanoparticles as drug delivery systems.....	10
2.3.1	Active and passive targeting.....	11
2.3.2	Surface modifications.....	12
2.3.3	Controlled drug release.....	13
2.3.4	Other usages of nanoparticles in medicine.....	14
2.4	RGD/RAD conjugated oil-in-water nanoemulsion.....	15
2.5	In vitro model.....	16
2.6	Saturation binding.....	16
2.7	Fluorescence and fluorophores.....	18
2.8	Flow Cytometry.....	20
<b>3</b>	<b>Materials and Methods.....</b>	<b>24</b>
3.1	Materials.....	24
3.1.1	RGD/RAD conjugated oil-in-water nanoemulsion.....	24
3.1.2	Antibodies.....	25
3.1.3	Cell cultivation.....	25
3.1.4	Laboratory instruments.....	26
3.2	Methods.....	27
3.2.1	Cell cultivation.....	27
3.2.2	RGD/RAD conjugated oil-in-water nanoemulsions.....	27
3.2.3	Analysis.....	28
3.2.4	Protocols.....	29
3.2.5	Antibody staining.....	31
3.2.6	Nanoemulsion incubation.....	32
3.2.7	Effect of trypsin on detached HUVEC.....	33
3.2.8	Saturation binding.....	35
<b>4</b>	<b>Results.....</b>	<b>37</b>
4.1	Optimization of integrin staining.....	37
4.2	Integrin expression as a function of cell density.....	38
4.3	Cellular uptake of RGD/RAD-NE as a function of cell density.....	40
4.4	Effect of trypsin on detached HUVEC.....	46
4.5	Saturation binding of RGD-NE at 37°C.....	48
4.6	Saturation binding of RGD/RAD-NE at 4°C.....	51
4.7	Comparison of $K_d$ .....	54
<b>5</b>	<b>Discussion.....</b>	<b>57</b>
5.1	Optimization of integrin staining.....	57
5.2	Integrin expression as a function of cell density.....	57
5.3	Cellular uptake rate of RGD-NE as a function of cell density.....	58
5.4	Effect of trypsin on detached HUVEC.....	61
5.5	Saturation binding of RGD-NE at 37°C.....	61
5.6	Saturation binding of RGD/RAD-NE at 4°C.....	62
5.7	Comparison of $K_d$ to the Kibria study.....	63
<b>6</b>	<b>Conclusion.....</b>	<b>64</b>

6.1 Thesis work .....	64
6.2 Future work .....	64
<b>Literature .....</b>	<b>66</b>

## Acknowledgements

This master thesis was carried out at the Norwegian University of Science and Technology, Department of Physics, Biophysics, Spring 2016.

Thanks to all of you at Biophysics, I have really enjoyed your company and I wish you the best of luck with your research. I would specially like to thank my supervisor Sjoerd Hak for excellent guidance throughout my thesis work. I have appreciated our close collaboration and that you always had time for my thesis and me. You are observant and have an incredible memory, a strong knowledge in your discipline and a great personality. Keep me updated on your project! Kristin G. Sæterbø, you are indispensable. In the beginning of my thesis work you guided me safely through cell laboratory work and training in Flow Cytometry. Thank you for your caring and positive nature. Linda Sønstevold, thank you for all your kind help and for always sharing your knowledge. Sofie Snipstad, you are a source of inspiration with your naturally hunger for new knowledge. I appreciate both your company and your input related to my thesis. I wish you the best of luck with finishing your PhD. Nils-Helge, I couldn't have done my thesis without your tremendous support. You have done an incredible job at home and cared for of our kids while I was studying. Thank you to my mother for having my husband and kids for visits and for taking very good care of them, as always. Thank you to my patient and adorable kids, Iver and Ellinor, who finally are going to get a more present mom. I am looking forward to spend the summer with you!



## Abstract

The purpose of this master thesis was to quantitatively study the binding and internalization of  $\alpha_v\beta_3$  integrin-targeted RGD-conjugated nanoemulsions (RGD-NE) by human umbilical vein endothelial cells (HUVEC) *in vitro*. The RGD-peptide sequence recognizes and binds specifically to  $\alpha_v\beta_3$ -integrins; receptors overexpressed in endothelial cells of angiogenic tumor vasculature and therefore a suitable target for nanomedicine.

RGD-NE was fluorescently labeled with Rhodamine-PE to detect cellular uptake.  $\alpha_v\beta_3$  integrin was stained with fluorescent-labeled antibodies to detect expression levels. Flow cytometry was utilized to quantitatively measure positive fluorescent HUVEC. Low density HUVEC (fast proliferating in lag phase) is expected to express high levels of  $\alpha_v\beta_3$  integrins, while high density HUVEC (non-proliferating) is expected to express low levels. Targeting rates and levels are expected to correlate with integrin expression levels. Based on these expectations we investigated  $\alpha_v\beta_3$  integrin expression and cellular uptake rates of RGD-nanoemulsions as function of cell density. An achievement of a distinct low and high density within the same cell line would possibly enhance the *in vitro* model.

Antibody staining experiments detected that the level of  $\alpha_v\beta_3$  integrins decreases with increasing cell density, thus providing the possibility to study targeting as a function of expression levels of the target. RGD-NE incubation showed a correlation between increasing time between seeding and experiment (seeding regime) and decreasing cellular uptake of RGD-NE. When comparing 2, versus 4, versus 9 days between seeding of high density HUVEC, the uptake of RGD-NE decreases with increasing number of days from seeding to the day of experiment. Integrin levels were measured to be very similar when comparing these different seeding regimes, so these findings have to be more thoroughly investigated before making a final conclusion. In an attempt to characterize the binding of the RGD-NE in a more quantitative manner, saturation studies were performed to make an estimate of the dissociation constant ( $K_d$ ), a measure of affinity binding. Preferably, the saturation binding studies should be performed at 4°C since the energy-dependent endocytosis will be inhibited and hence the result will reflect only bound and not internalized RGD-NE. The experimental set-up has to be further developed and optimized for a more reliable and significant result.

# 1 Introduction

Cancer represents a leading cause of death worldwide. *Cancer* refers to cells that grow out of control and invade other tissues. Cells become cancerous due to the accumulation of defects, or mutations, in their DNA. Most of the time, cells are able to detect and repair DNA damage. If a cell is severely damaged and cannot repair itself it undergoes so-called programmed cell death or apoptosis. Cancer occurs when damaged cells grow, divide, and spread abnormally instead of self-destructing, as they should. [1] To increase cancer survival rates, there is a strong need for earlier detection and more specific cancer therapies than what we have today. The use of nanoparticles is a novel approach in cancer therapy and diagnostics, which shows potential to achieve this. [2] *Nanomedicine* is defined as the application of nanotechnology in medicine. Nanomedicine has the potential to provide improved efficacy, bioavailability, dose–response, targeting ability, personalization, and safety compared to conventional medicines. One nanometer equals 0.000000001 meters, i.e.  $10^{-9}$  meter. [3] Anti-cancer and contrast agents may be incorporated in nanoparticles, and the nanoparticles may be directed to interact only with specific cells and tissue, e.g. by the conjugation of targeting ligands. [2] One type of nanoparticles to use within medicine for drug delivery and molecular imaging is oil-in-water nanoemulsion, which consists of a lipid core surrounded by cholesterol, DSPE and PEG-DSPE. The design of the nanoemulsion allows for various compounds to be incorporated, such as imaging agents and/or hydrophobic drugs. [4] RGD-conjugated nanoemulsion and RAD-nanoemulsion (control emulsion) was synthesized and utilized in this thesis to target  $\alpha_v\beta_3$  integrin, overexpressed in tumor angiogenic endothelial cells.

The overall aim of this thesis was to further study the targeting kinetics of RGD-conjugated nanoemulsion to  $\alpha_v\beta_3$  integrin, since it is a well-known target, both *in vitro* and *in vivo*. Specifically in this thesis, the purpose was to quantitatively:

- Investigate the integrin expression levels as a function of cell density, to gain a better understanding of the target
- Examine if cellular uptake of nanoemulsions correlates to cell density and integrin expression
- Study how well the targeted nanoemulsion binds to the target, by developing an approach to estimate  $K_d$



## 2 Theory

### 2.1 Hallmarks of cancer

Hanahan et al. suggest that the vast catalog of cancer cell genotypes is a manifestation of six essential alterations in cell physiology that collectively dictate malignant growth (see figure 1): self-sufficiency in growth signals, insensitivity to growth-inhibitory (antigrowth) signals, evasion of programmed cell death (apoptosis), limitless replicative potential, sustained angiogenesis, and tissue invasion and metastasis. Each of these physiologic changes, novel capabilities acquired during tumor development, represents the successful breaching of an anticancer defense mechanism hardwired into cells and tissues. Conceptual progress in the last decade has added two emerging hallmarks of potential generality to this list, *reprogramming of energy metabolism* and *evading immune destruction*. [5] These capabilities are shared in common by most and perhaps all types of human tumors. This multiplicity of defenses may explain why cancer is relatively rare during an average human lifetime. [6]

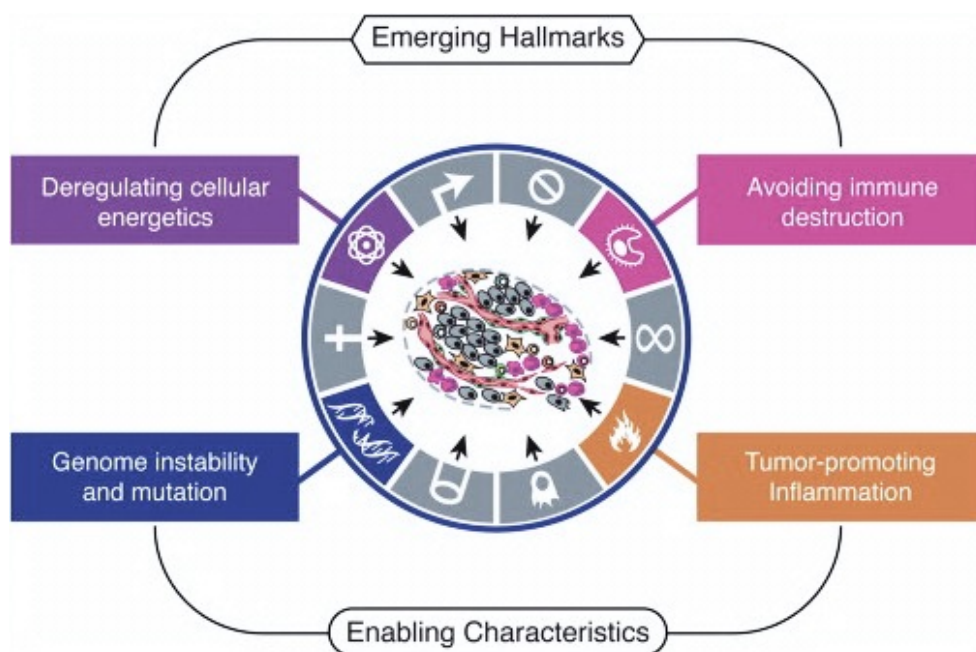


**Figure 1:** Acquired capabilities of cancer cells. [5]

### 2.1.1 Targeting angiogenesis

One of the hallmarks of cancer is *sustained angiogenesis*. Oxygen and nutrients supplied by the vasculature are crucial for cell function and survival, obligating virtually all cells in a tissue to reside within 100 $\mu$ m of a capillary blood vessel. During organogenesis, this closeness is ensured by coordinated growth of vessels and parenchyma. Once a tissue is formed, the growth of new blood vessels, the process of angiogenesis, is transitory and carefully regulated. Counterbalancing positive and negative signals encourage or block angiogenesis. One class of these signals is conveyed by soluble factors and their receptors, the latter displayed on the surface of endothelial cells; integrins and adhesion molecules mediating cell-matrix and cell-cell association also play critical roles. The angiogenesis-initiating signals are exemplified by vascular endothelial growth factor, VEGF, and acidic and basic fibroblast growth factors, FGF1/2. Each binds to transmembrane tyrosine kinase receptors displayed by endothelial cells. [6]

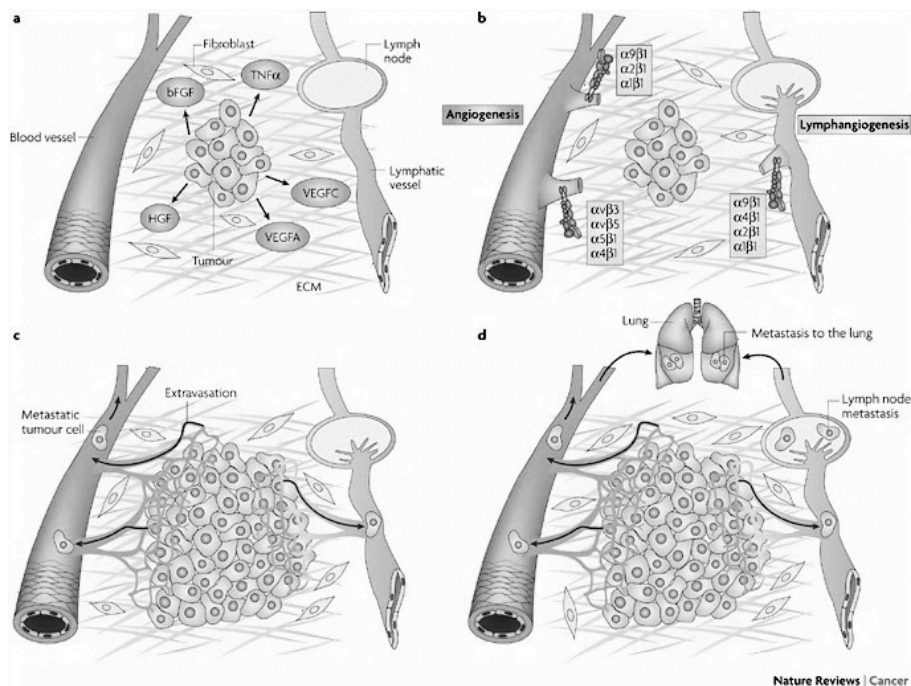


**Figure 2:** Illustration adapted from Nature Reviews Cancer [7].

- a. Tumor cells near pre-existing blood vessels secrete growth factors and chemokines, such as vascular endothelial growth factor A (VEGF-A), basic fibroblast growth factor (bFGF) and tumor necrosis factor (TNF) that stimulate quiescent vascular endothelium

to enter the cell cycle. Tumors also secrete factors that stimulate the growth of new lymphatic vessels. [7]

- b. These growth factors activate or up-regulate expression of *integrins* on blood- and lymphatic vessels. [7]
- c. These integrins then promote endothelial cell migration and survival during invasion of tumor tissue, resulting in the creation of new vessel sprouts. The new blood vessels promote tumor growth by removing waste products and providing nutrients. These new blood and lymphatic vessels also provide an avenue for tumor metastasis. [7]
- d. Lymphangiogenesis promotes metastasis to lymph nodes and, sometimes, more distant tissues such as lung, whereas angiogenesis promotes metastasis to local and distant sites, such as the lungs. [7]

## 2.2 Integrins

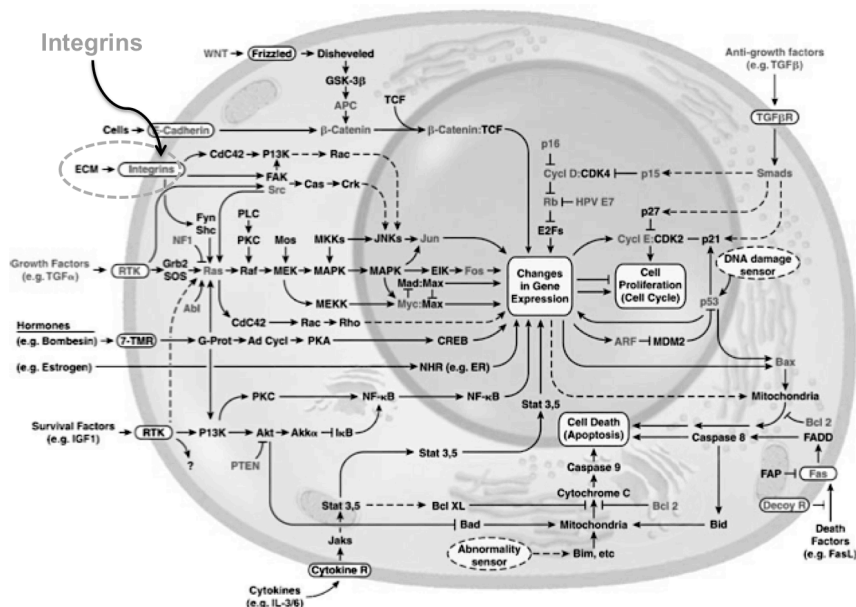


**Figure 3:** Signaling pathways in a cell. Illustration adapted from Cell Press: Hallmarks of cancer [6]

Integrins are transmembrane receptors in form of a heterodimer consisting of an alpha ( $\alpha$ ) and a beta ( $\beta$ ) unit, with a large extracellular domain and a short intracellular tail. Until now, 24

distinct integrin heterodimers composed of various combinations of the 18  $\alpha$ - and 8  $\beta$ -units has been found. [8] Signals transmitted by integrin heterodimers and their associated molecules play fundamental roles in processes such as cell migration, proliferation, and apoptosis. Dysfunction in these processes can lead to diseases such as cancer. The cellular mechanisms regulating integrin function are hence of considerable interest. [6, 9]

Integrins are involved in interactions between the cell and the surrounding extracellular matrix, *ECM*. *ECM* is a network of secreted proteins that largely fills the extracellular milieu of many tissues and organs and provides structural support for cells. [10] Integrin heterodimers can adopt a bent and closed conformation that has a low affinity for ligand or an extended and open conformation that has a high affinity for ligands. As a consequence of this conformational switching, integrins are able to signal bi-directionally across the membrane. Ligand binding produce signal responses within the cell, while binding of intracellular proteins to integrins promotes binding of ligand. [8]

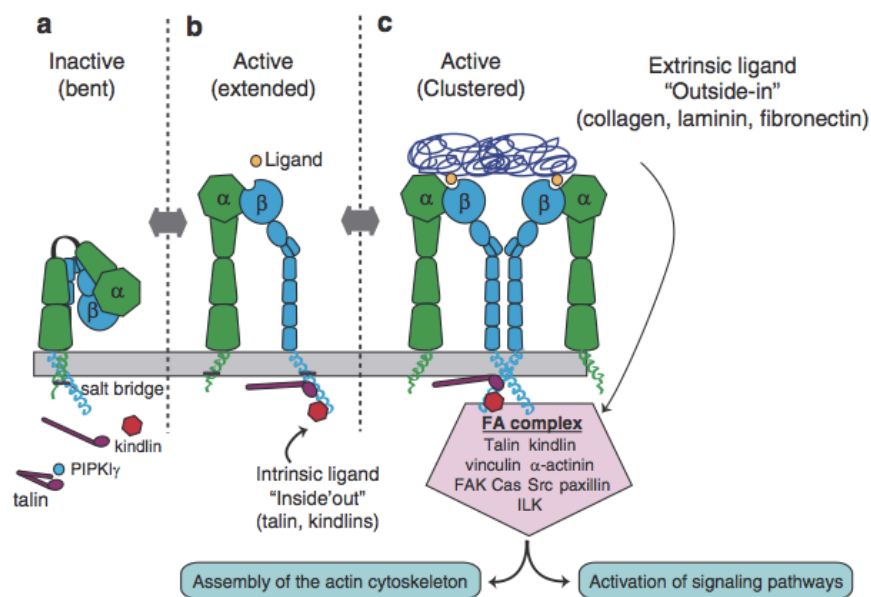


**Figure 4:** **a** Integrins in their unbound, inactive resting state. In this state integrins are in a bent conformation and the transmembrane and cytoplasmic regions are closely associated. **b** Once activated by talins and kindlins, there is separation of the cytoplasmic and transmembrane subunits and extension of the integrins extracellular domains. Extracellular ligand binding can occur in this conformation. **c** When activated integrins bind to ligand, they cluster at the plasma membrane. Clustering is necessary to send intracellular signals to form tight focal adhesions (FA), important for actin cytoskeletal assembly and activation of further downstream signals to control various cellular functions. [11]

Integrin follow endocytosis by clathrin-independent, *clathrin*- or *caveolin* dependent mechanisms. Newly identified internalization pathways include macropinocytosis from

circular dorsal ruffles (CDRs), see figure 5. Integrins then travel to early endosomes where the sorting decisions are made to determine whether receptors are sent to late endosomes and lysosomes for degradation or are recycled by one of two spatially and temporally distinct routes, referred to as *short-loop* and *long-loop* pathways. Generally, integrins are not degraded but are efficiently recycled to the plasma membrane either by a RAB4-dependent route (short loop) or by moving to the *perinuclear recycling compartment* before returning to the plasma membrane through mechanisms requiring RAB11 and/or ADP-ribosylation factor 6 (ARF6) (long loop). [9, 10, 12] These recycling pathways facilitate adhesion turnover and provide the cell with a constant fresh pool of integrins to engage the matrix and generate new adhesions. [12]

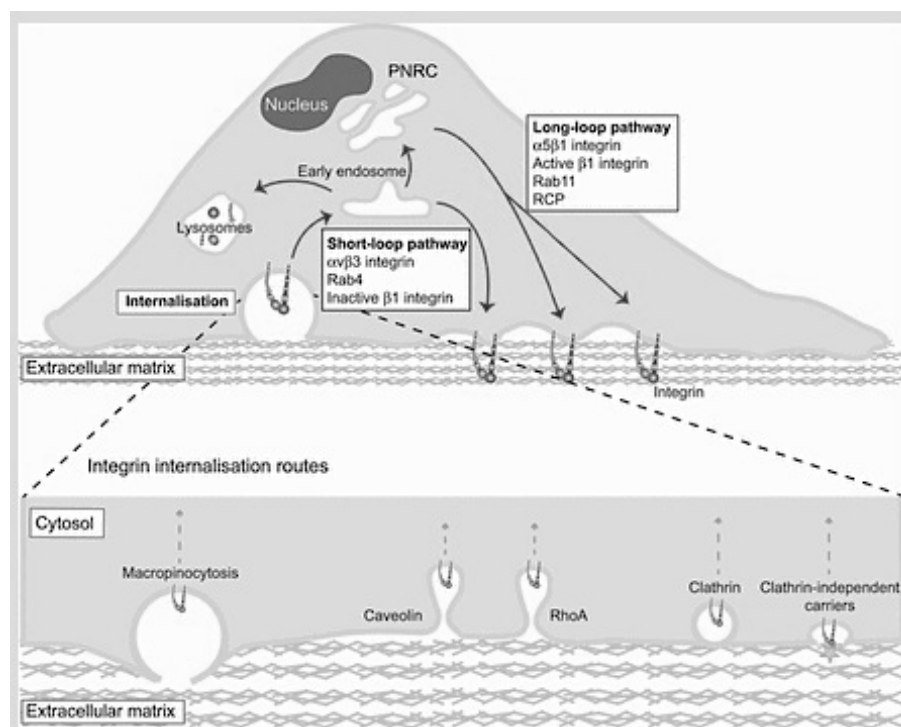


**Figure 5:** Illustration of integrin internalization routes and recycling pathways, described as *short loop* and *long loop*. [12]

## 2.2.1 $\alpha_v\beta_3$ -integrin

$\alpha_v\beta_3$  integrins controls receptor trafficking, suppressing the recycling of  $\alpha_5\beta_1$  integrin, and thereby leads to changes in Rho GTPase signaling in fibroblasts and promotes receptor-

tyrosine kinase trafficking and signaling in carcinoma cells. Inhibiting  $\alpha_v\beta_3$  with small molecule inhibitors such as Cilengitide in endothelial cells drives Rab4- dependent vascular endothelial growth factor receptor 2 (*VEGFR<sub>2</sub>*) recycling, protecting this receptor from degradation in the presence of VEGF ligand and increasing its levels on the cell surface. This promotes VEGF-driven endothelial cell migration, sprouting of aortic explants and tumor angiogenesis in vivo, which ultimately lead to enhanced growth of the tumor. [8]

Integrin heterodimers of the  $\beta_1$  and  $\beta_3$  classes are internalized via mechanisms that depend on dynamin and PKC- $\alpha$ , but are most likely to be clathrin-independent. All of this traffic proceeds to early endosomes, *EEs*, then to the perinuclear recycling compartment, *PNRC*, and finally returns to the plasma membrane via a 'long-loop' of recycling requiring Rab11. The transport of  $\alpha_5\beta_1$ ,  $\alpha_v\beta_3$  and  $\alpha_6\beta_4$  via the 'long-loop' is dependent, not only on Rab11 but also on the activity of the PKB/GSK-3 $\beta$  axis.  $\alpha_v\beta_3$  and the TFN-R can also return to the plasma membrane without passing through the PNRC, thus completing a 'short-loop' of internalization and recycling. The transport of  $\alpha_v\beta_3$  integrin via the short loop additionally requires the recruitment of PKD1 as indicated and only occurs following treatment of fibroblasts with PDGF. The  $t_{1/2}$  of transport of  $\alpha_v\beta_3$  integrin from *EEs* to the plasma membrane is approximately 3 min, and the delivery of  $\alpha_5\beta_1$  and  $\alpha_v\beta_3$  integrins from the PNRC to the plasma membrane has  $t_{1/2}$  of approximately 10 minutes. [9]

Several  $\alpha_v\beta_3$  integrin ligands have been successfully used as targeting ligands for molecular imaging in cancer angiogenesis. Radiolabeled  $\alpha_v\beta_3$  integrin antibodies have allowed for the detection of  $\alpha_v\beta_3$  integrin expressing cancer. Other widely used targeting ligands for  $\alpha_v\beta_3$  integrin are RGD or RGD-based peptides. It has been long known that integrins bind to proteins expressing the RGD-sequence. This realization led to an enormous effort to develop RGD based ligands for  $\alpha_v\beta_3$  integrin-targeting and it has been found that cyclic pentapeptides containing RGD showed very high affinity for  $\alpha_v\beta_3$  integrin. Furthermore, RGD multivalency further increases the specificity for integrin. Radiolabeled RGD or RGD-based peptides have been widely demonstrated to allow for in vivo detection of tumor associated  $\alpha_v\beta_3$  integrin expression. Several of such agents have entered clinical trials and show promising potential for minimally invasive  $\alpha_v\beta_3$  integrin detection. [13]

### 2.3 Nanoparticles as drug delivery systems

The use of nanoparticles as carriers for drug delivery is a rapidly growing field of research. There are several advantages of using drug carriers within the nanoscale, such as increased drug circulation times, increased drug concentration at the disease site, minimal drug degradation and loss, and ease of administration. [14] Drug delivery systems, *DDS*, administrate drugs through controlled delivery so that an optimum amount reaches the target site. Drug delivery systems encompass the carrier, route and target. [15] In traditional medication only 0.001 to 0.01% of the medicine is delivered to the diseased area, while the remaining drug is delivered where it is not required, possibly creating toxicity or negative effects. [16]

The overall aim for using a DDS is to improve bioavailability and pharmacokinetics. A drug delivery system will improve solubility of poorly water-soluble drugs, prolong half-life of drug systemic circulation by reducing immunogenicity, allow drug release at sustained rate or in an environmentally responsive manner and allow drug delivery in a targeted manner. To be able of co-delivery of two or more drugs simultaneously for combination therapy and to generate a synergistic effect and suppress drug resistance, is another advantage of a DDS. A drug delivery system may be surface functionalized with targeting ligands or “stealth” structures to further increase their specificity and efficacy. “Stealth” structures may increase the ability to cross biological barriers or enable passive targeting of tissues. [15] In general, the use of DDS to deliver drugs in the optimum dosage for long periods to increase efficacy, maximize patient compliance and enhance ability to use highly toxic, poorly soluble or relatively unstable drugs. Ideally, the DDS should extend blood circulation, deliver at the target site and bypass the endosome-lysosome processing. Therefore, the systemic side effects may be minimized, lower therapeutic toxicity. The frequency of administration may be lowered. Effective and/or more convenient routes of administration are possible; so the product life cycle may be extended. Ultimately health-care costs will be reduced and more patient-friendly and personalized therapy is possible. [15]

Nanoparticles have sizes similar to biological entities such as proteins and viruses, and can therefore interact with biomolecules on the cell surface and within the cell. It is also important that the use of nanoparticles allows for controlled drug release at the disease site, as well as the possibility for specific cell targeting. Dimensions of nanocarriers are usually between 10

nm and 200 nm. Depending on the nanocarrier, the drug can be captured inside the particle using different techniques and can be retained with different interactions (*e.g.* covalent and electrostatic interactions). As such, not every drug is compatible with every type of nanoparticle. There are many different kinds of nanoparticles such as polymeric nanoparticles, liposomes, carbon nanotubes, dendrimers, micelles and several others (figure 6). Depending on the material used and modifications on the surface, nanocarriers can have different properties and drug release characteristics. [14]

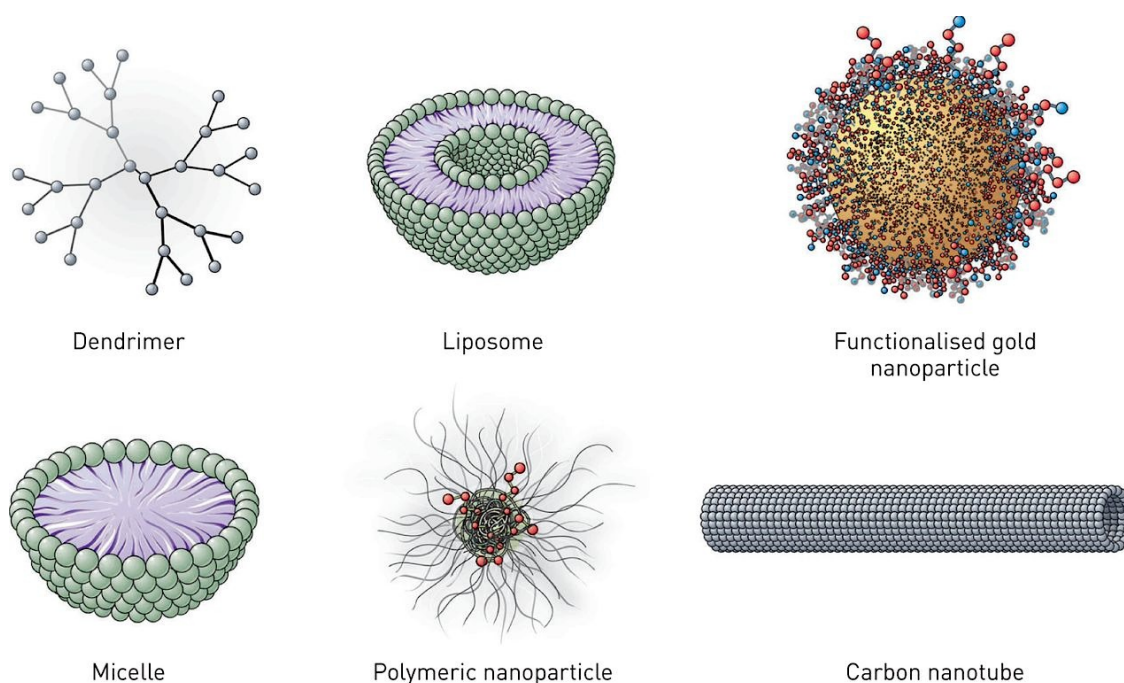


**Figure 6:** Examples of nanoparticles commonly used as drug delivery systems. [14]

### 2.3.1 Active and passive targeting

Nanoparticles also offer the possibility for specific tissue or cell targeting, which has the potential to greatly increase their therapeutic effect and decrease drug toxicity. Both *active* and *passive* nanoparticle-based targeting is possible.

Passive accumulation of nanoparticles in tumor tissue is observed due to a phenomenon known as the enhanced permeability and retention, *EPR* effect. This is caused by the insufficient drainage and poorly regulated angiogenesis of tumors, resulting in an unstructured and leaky vasculature [17] Passive targeting can also be achieved by surface charge of



nanoparticles. [14] The physiology of diseased tissues is altered through a variety of conditions, one of them being the enhanced permeability and retention, *EPR*, effect. Because tumor vasculature is leaky, circulating nanoparticles can accumulate more in the tumor tissues than in normal tissues. The *EPR* effect is also observed at the site of inflammation. The only difference between inflammation-induced *EPR* effect and that of cancer is duration of retention period. The retention in normal tissue, where inflammation occurs, is shorter than with cancer because the lymphatic drainage system is still operative. [15]

Active targeting can be achieved by attaching targeting ligands to the surface of nanocarriers that bind to molecules specific for the diseased cell (*i.e.* cell receptors that are over-expressed or cell type specific). For example, integrins are transmembrane receptors that mediate interactions with the surrounding extracellular matrix and are up regulated in proliferating tumors cells. [18] Integrin targeting liposomes loaded with doxorubicin inhibited tumor progression in a colon carcinoma mouse model, whereas non-targeting liposomes were ineffective. [19] Several other examples of successful integrin-specific binding of nanoparticles exist. [20] Cell type-specific targeting can be achieved by conjugating nanoparticles with cell adhesion antibodies. [21] Active targeting requires conjugation of receptor specific ligands that can promote site specific targeting. The success of drug targeting depends on the selection of the targeting moiety, which should be abundant, have high affinity and specificity of binding to cell surface receptors and should be well suited to chemical modification by conjugation. The active targeting can be achieved by molecular recognition of the diseased cells by various signature molecules overexpressed at the diseased site either via the ligand-receptor, antigen-antibody interactions or by targeting through aptamers. [15]

### **2.3.2 Surface modifications**

Most particles allow for surface modifications that can positively affect their bio distribution and circulation times. The hydrophobicity determines, to a large degree, the level of particle binding to blood components. Non surface-modified hydrophobic particles are removed from the circulation more rapidly. [14] To increase the blood circulation time of such particles, they can be coated with hydrophilic polymers or surfactants. For example, low molecular weight

poly(ethylene glycol) (PEG) chains that decorate the particle in a brush-like fashion (PEGylation) are known to reduce phagocytosis [22]

### 2.3.3 Controlled drug release

Controlled release of the drug from the particle is also essential for therapeutic success. Release from the particles can either be stimuli responsive or sustained. Most polymeric and liposome particles have sustained or continuous release of the drug by either diffusion out of the particle or slow degradation of the particle over time. Stimuli-responsive drug release may result in a more targeted release of the drugs and can be achieved by a change in biological environment, such as reducing environment of the cell, change of pH or altered levels of disease-specific enzymes. [14] Another example of responsive drug release is represented by PEG-peptide-lipid conjugates, where the PEG molecules could be removed from the carriers *via* cleavage by matrix metalloproteinases that are overexpressed in tumor tissues. [23] External physical stimuli such as light, ultrasound, heat and electric or magnetic fields may also be used to achieve controlled drug release. One example of such an approach is the use of ultrasound-sensitive micro bubbles for local release of drugs. [24]

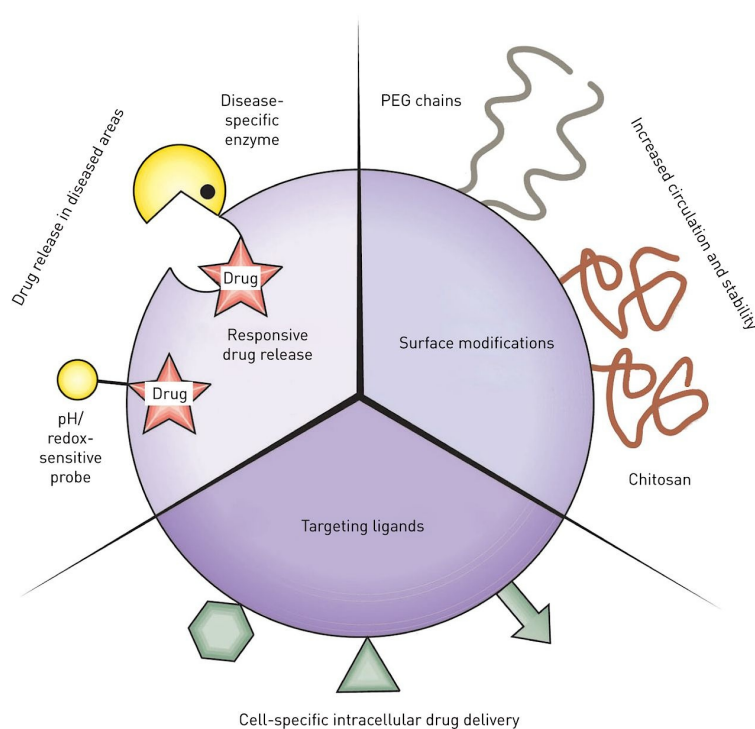


**Figure 7:** Schematic diagram to summarize different properties that are important for the design of nanocarriers for drug delivery. PEG: poly(ethylene glycol). [14]

## 2.3.4 Other usages of nanoparticles in medicine

### 2.3.4.1 Molecular imaging

The development of the effective carrier system does not only mean the execution of delivery, but also the positive confirmation of the site-specific delivery of the drug. Consequently, the ability to track and image the fate of any nanomedicine from the systemic to the subcellular level becomes essential. Nanoparticles can be successfully exploited to improve the utility of fluorescent markers (see section 2.7) for medical imaging and diagnostic purposes. Although various fluorescent markers are widely used in research and clinical diagnostic applications, current techniques have several disadvantages, such as the requirement of color-matched lasers, fluorescence bleaching and lack of discriminatory capacity of multiple dyes, etc. Fluorescent nanoparticles can greatly overcome these problems and a major advance toward clinical applicability is the use of nanoparticles to image tumors and other diseases in vivo. [15]

### 2.3.4.2 Theranostics

*Theranostics* refers to the simultaneous integration of diagnosis and therapy. Theranostic nanoparticles are multifunctional nanoparticle complexes that can simultaneously deliver diagnostic and therapeutic agents to targeted sites. Nanotheranostics is to apply and further develop nanomedicine strategies for advanced theranostics, *i.e.* to apply and further develop the various nanocarriers for sustained, controlled and targeted co-delivery of diagnostic and therapeutic agents for better theranostic effects and fewer side effects. The purpose is to diagnose and treat the diseases at their earliest stage, when the diseases are most likely curable or at least treatable. Theranostic nanomedicine means colloidal nanoparticles ranging in sizes from 10 to 1000 nm (1 $\mu$ m). [3]

## 2.4 RGD/RAD conjugated oil-in-water nanoemulsion

Lipid-based nanoparticles consists of primarily amphiphilic lipids, which in an aqueous environment spontaneously aggregate into e.g. micelles, liposomes and nanoemulsions. Amphiphiles are molecules that contain both a hydrophobic (non-polar) and a hydrophilic (polar) domain. In these self-associated aggregates, the hydrophobic domains are clustered and thus minimizing contact with water. The hydrophilic domains form hydrogen bonds with surrounding water molecules. [13] The amphiphilic lipids used in the nanoemulsions in this thesis work are DSPC, Cholesterol and MAL-PEG-DSPE.

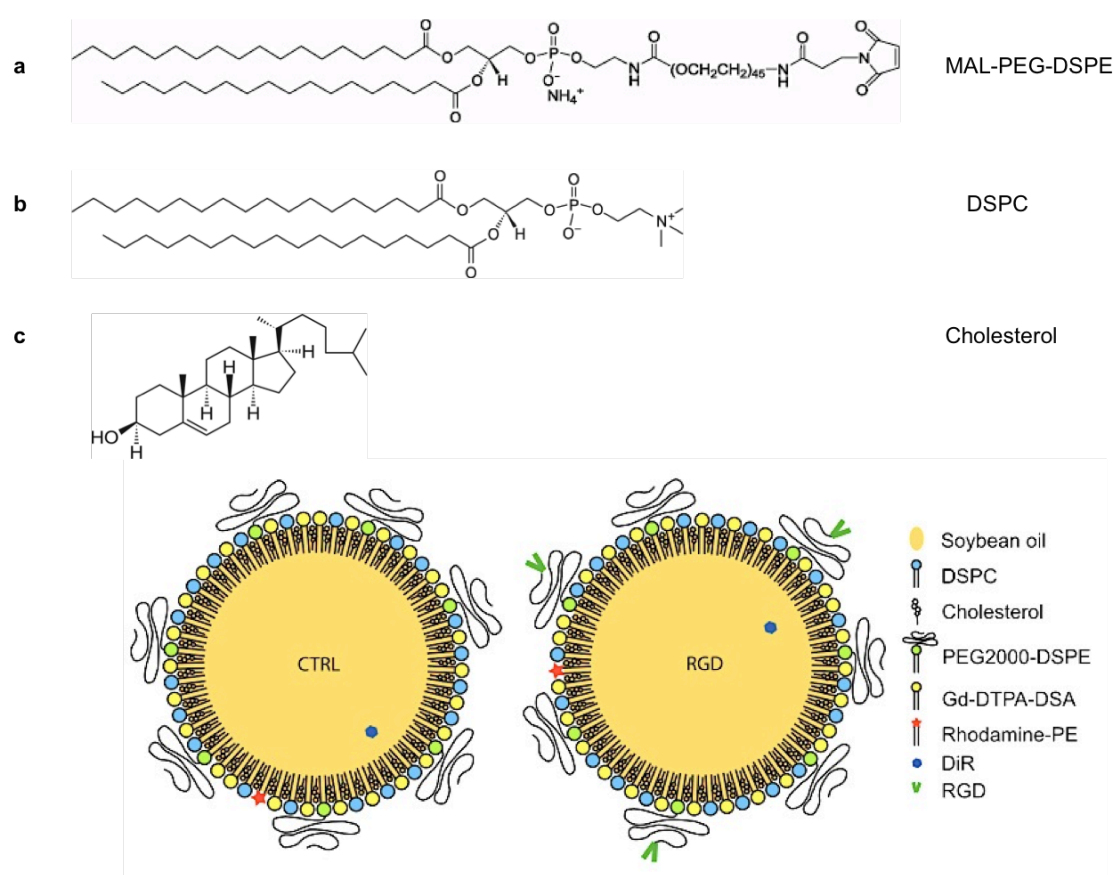


**Figure 8:** a: MAL-PEG-DSPE, b: DSPC and c: Cholesterol. RGD conjugated nanoemulsion. CTRL: RAD conjugated control nanoemulsion. [13]

Nanoemulsion conjugated with RAD peptide works as a control emulsion. The substitution of glycine (G) with alanine (A) makes the peptide inactive when it comes to  $\alpha_v\beta_3$  binding. The RAD peptide sequence is therefore a strong negative control for investigating the biological activity mediated by  $\alpha_v\beta_3$  integrin. [25]

## 2.5 In vitro model

For development and investigation of potential new therapeutic and diagnostic approaches, initial experiments are often performed *in vitro* with cells in culture. The use of *in vitro* experiments is necessary to reduce the extent of animal testing, which is important due to ethical constraints, and to reduce cost and time consumption. However, an important limitation for *in vitro* experiments is that the cellular environment in a culture dish differs significantly from the *in vivo* cellular environment. [26] Therefore, cellular responses observed *in vitro* are not necessarily representative for cellular responses *in vivo*.

In this project, cultured human umbilical vein endothelial cells, *HUVEC*, were utilized as an *in vitro* model system to study  $\alpha_v\beta_3$  integrin targeting. HUVEC, grown in cell culture, display many of the characteristics of angiogenic endothelial cells, including expression of  $\alpha_v\beta_3$ -integrins. [27] HUVEC are adherent cells. Growths of cultured cells begin with the lag phase after seeding, where adherent cells adhere to the new substrate. Next the log phase follows, where cells proliferate exponentially. At one point, the adherent cells will occupy all available substrate. Hence, the cells have no space left for expansion, and proliferation is greatly reduced or ceased entirely. The phase of cell growth is important for experiments investigating the  $\alpha_v\beta_3$ -integrin in cultured HUVEC, because expression of  $\alpha_v\beta_3$ -integrin is kept up regulated in proliferating endothelial cells *in vitro*, while non-proliferating endothelial cells express  $\alpha_v\beta_3$  at low levels. [28]

## 2.6 Saturation binding

Binding is the first step necessary for a biological response. We have to examine how binding is affected by ligand and macromolecule concentrations, and how to experimentally analyze and produce binding curves to understand saturation binding. [29] Sites available for binding are limited by the concentration of bound drug. The ability to saturate refers to when a process fails to increase in direct proportion to dose or concentration and approaches an upper limit. [30]

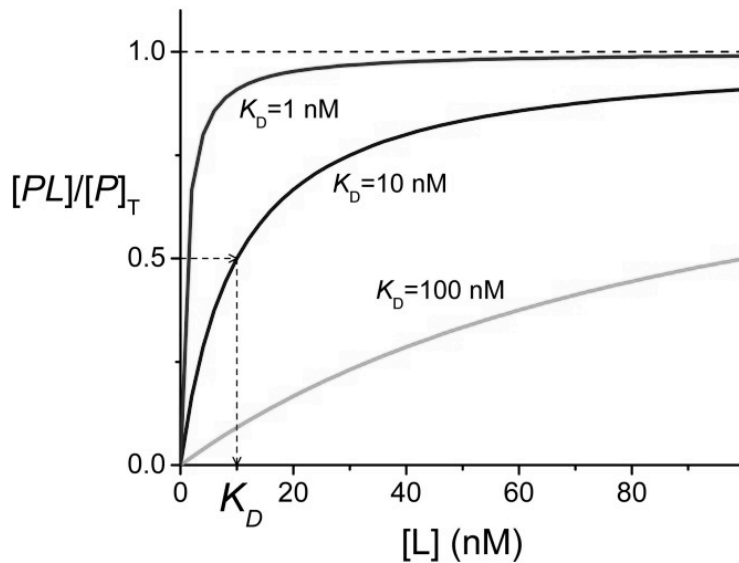


**Figure 9:** The figure shows different values of dissociation constant,  $K_d$ . The steeper the rise of the curve, the lower  $K_d$  and thus higher affinity for the complex binding: Protein + Ligand (PL).  $(P)_T$  is maximal binding sites available [31]

The dissociation constant,  $K_d$  describes ligand concentration, in this thesis, the concentration of [RGD-NE] at half maximal binding. [29] The binding curves changes accordingly to changes in  $K_d$ . The lower the  $K_d$ , i.e. the higher concentration of binding complexes of RGD-NE and  $\alpha_v\beta_3$  integrin, the tighter the binding. The higher the value of  $K_d$ , the looser the complex binding of RGD-NE and receptor  $\alpha_v\beta_3$  integrin.

Within the world of drugs, the degree of plasma protein binding is frequently expressed as the bound-to-total concentration ratio, with limiting values between 0 and 1. Drugs with values greater than 0.9, are said to be extensively bound. Unbound, rather than bound, concentration is more important in therapeutics. Binding is described a function of the affinity of the protein for the drug. Affinity is characterized by an association constant  $K_a$ .  $K_a$  is the inverse constant of  $K_d$ , the dissociation constant. Because the number of binding sites on a protein is limited, binding also depends on the molar concentrations of both drug and protein. For a single binding site on the protein, the association is simply summarized by the following reaction:

Drug + Protein  $\rightleftharpoons$  Drug-Protein complex. High affinity implies that equilibrium lies far to the right. This is a relative statement, as the greater the protein concentration for a given drug concentration, the greater the bound drug concentration and the converse. [30]

## 2.7 Fluorescence and fluorophores

Fluorescent molecules, also called fluorophores or simply fluors, respond distinctly to light compared to other molecules. As shown below, a photon of excitation light is absorbed by an electron of a fluorescent particle, which raises the energy level of the electron to an excited state. During this short excitation period, some of the energy is dissipated by molecular collisions or transferred to a proximal molecule, and then the remaining energy is emitted as a photon to relax the electron back to the ground state. Because the emitted photon usually carries less energy and therefore has a longer wavelength than the excitation photon, the emitted fluorescence can be distinguished from the excitation light. The excitation and photon emission from a fluorophore is cyclical, and until the fluorophore is irreversibly damaged (photobleaching) it can be repeatedly excited. Because fluorophores can emit numerous photons through this cycle of excitation and emission, fluorescent molecules are used for a broad range of research applications. [32]

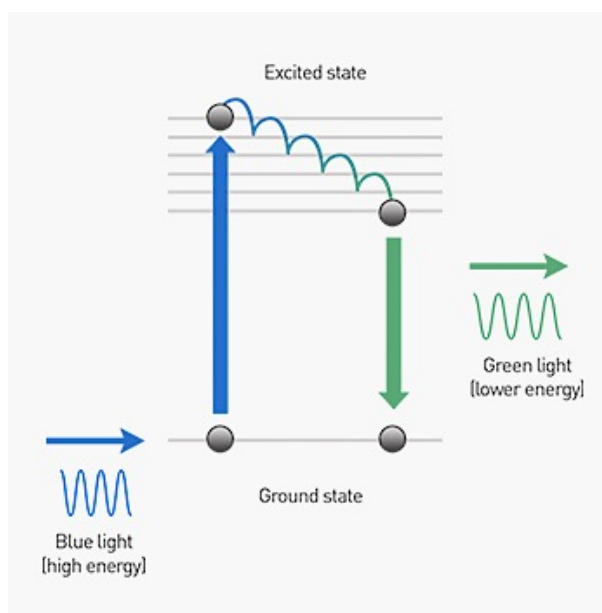


**Figure 10:** Jablonski energy diagram of fluorescence. [33]

The distance between the excitation and emission wavelengths is called the *Stokes Shift* (see figure 11 below) and is a key aspect in the detection of the emitted fluorescence in biological applications. The Stokes shift is also a distinct characteristic of each fluorophore. For example, the detection of emitted fluorescence can be difficult to distinguish from the excitation light when using fluorophores with very small Stokes shifts (left panel), because the excitation and emission wavelengths greatly overlap. Conversely, fluorophores with large

Stokes shifts (right panel) are easy to distinguish because of the large separation between the excitation and emission wavelengths. The Stokes shift is especially critical in multiplex fluorescence applications, because the emission wavelength of one fluor may overlap, and therefore excite, another fluor in the same sample. [32]

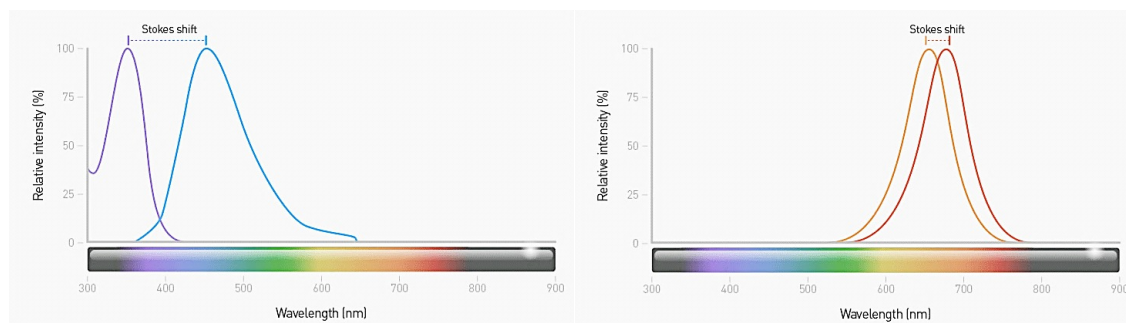


**Figure 11:** Stokes shift. [33]

Fluorophores can be divided into three general groups: organic dyes (e.g. Rhodamine), biological fluorophores (e.g. green fluorescent protein, GFP) and quantum dots. *Organic dyes* are small sized fluors, and this is a benefit over biological fluorophores because they can be conjugated to macromolecules, such as antibodies, without interfering with the biological function. The benefit of *biological fluorophores* is that expression plasmids can be introduced into either bacteria, cells, organs or whole organisms, to drive expression of that fluorophore either alone or fused to a protein of interest in the context of the biological processes studied. The size of the fluorescent protein can change the normal biological function of the cellular protein to which the fluorophore is fused, and biological fluorophores do not typically provide the level of photostability and sensitivity offered by synthetic fluorescent dyes. Quantum dots are nanocrystals (2-50nm) that provide tight control over the spectral characteristics of the fluor. There is greater specificity for distinct excitation and emission wavelengths than other fluors. Quantum dots have also been reported to be more photostable than other fluorophores. Additionally; quantum dots can be coated for use in different biological applications such as protein labeling. While the use of quantum dots in biological applications is increasing, there are reports of cell toxicity in response to the breakdown of the particles and their use can be cost-prohibitive. [32]

*Fluorescent microscopes* detect localized fluors in samples in both two and three dimensions. *Fluorescence scanners, e.g. microarray readers* detect localized fluors in samples in two



dimensions. *Spectrofluorometers and microplate readers* record the average fluorescence in samples, while *Flow cytometers* analyze the fluorescence of individual cells in a sample population. [32]

*Fluorescent labeling* is the process of covalently attaching a fluorophore to another molecule, such as a protein or nucleic acid. This is generally accomplished using a reactive derivative of the fluorophore that selectively binds to a functional group present in the target molecule. The most commonly labeled molecules are antibodies, which are then used as specific probes for the detection of a particular target. *Fluorophore conjugation* is when a chemically reactive derivative of a fluorophore is required for labeling molecules, e.g. sulfhydryl-reactive maleimide-activated fluors such as fluorescein-5-maleimide. [32]

Fluorophore detection in a given experiment can be obscured by high background fluorescence, which is most commonly caused by insufficient removal of nonbound fluorescent probe or sample *autofluorescence* (endogenous fluorescence of components in a sample). Thorough washing or a reduction in the concentration of fluorescent probe can reduce background fluorescence. [32]

## **2.8 Flow Cytometry**

*Flow* is motion, *cyto* is cell and *metry* is measurement. Flow cytometry is a technology that simultaneously measures and then analyzes multiple physical characteristics of single particles, usually cells in suspension, as they flow in a fluid stream and one by one passing through a beam of light. [34] A flow cytometer is used both in research and in clinical laboratories for disease profiling. Fluorescence is the generally used optical response. [35] The properties measured include a particle's relative size, relative granularity or internal complexity, and relative fluorescence intensity. These characteristics are determined using an optical-to-electronic coupling system that records how the cell or particle scatters incident laser light and emits fluorescence. A flow cytometer is made up of three main systems: *fluidics*, *optics* and *electronics*. The fluidics system transports particles in a stream to the laser beam for interrogation. The optics system consists of lasers to illuminate the particles in the sample stream and optical filters to direct the resulting light signals to the appropriate

detectors. The electronics system converts the detected light signals into electronic signals that can be processed by the computer. [34]

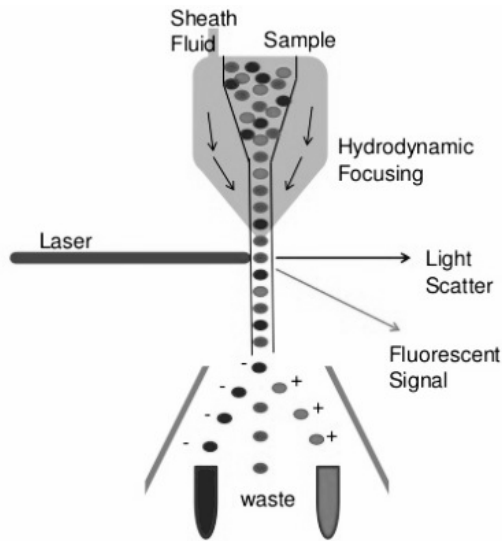


**Figure 12:** Sheath fluid focuses the cell suspension, causing cells to pass through a laser beam one cell at a time, called *hydrodynamic focusing*. Forward and side scattered light is detected, as well as fluorescence emitted from stained cells. [36]

One of the fundamentals of flow cytometry is the ability to measure the properties of individual particles. When a sample in solution is injected into a flow cytometer, the particles are randomly distributed in three-dimensional space. The sample must therefore be ordered into a stream of single particles that can be interrogated by the machine's detection system. This process is managed by the *fluidics system*. Essentially, the fluidics system consists of a central channel through which the sample is injected, enclosed by an outer sheath fluid that contains faster flowing fluid. The effect creates a single file of particles and is called hydrodynamic focusing. Under optimal conditions the fluid in the central chamber will not mix with the sheath fluid. After hydrodynamic focusing, each particle passes through one or more beams of light. Light scattering or fluorescence emission, if the particle is labeled with a fluorophore, provides information about the particle's properties. [37]

As the fluorescent cell passes through the laser beam, it creates a peak or pulse of photon emission over time. These are detected by the Photomultiplier tubes, *PMT*, and converted to a voltage pulse, known as an event. The total pulse height and area is measured by the flow cytometer. The measured voltage pulse area will correlate directly to the intensity of fluorescence for that event. The *PMT* measures the pulse area of the voltage created each time a fluorescing cell releases photons. When no fluorescing cells pass through the optics, no

photons are emitted and no signal is detected. As the fluorescent-labeled cell passes through the optics and is interrogated by the laser, photons are emitted and so the intensity of the voltage measured increases. As each fluorescing cell completes its path through the laser beam, this leaves a pulse of voltage over time.

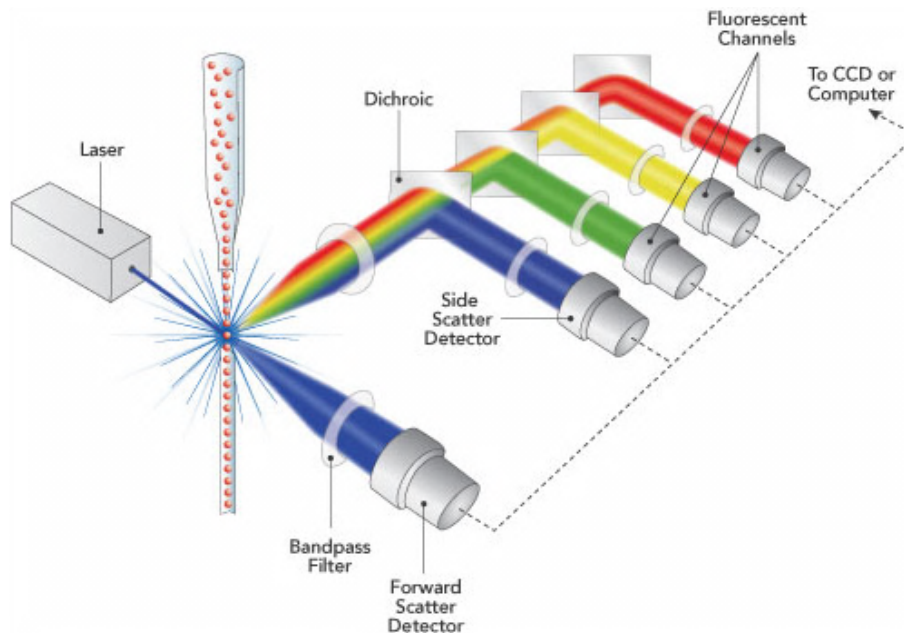


**Figure 13:** Schematic illustration of Flow cytometry. [38]

Cells or particles passing through the beam scatter light, which is detected as *forward scatter*, FS and *side scatter*, SS. FS correlates with cell size and SS is proportional to the granularity of the cells. In this manner, cell populations can often be distinguished based on differences in their size and granularity alone. As well as separating cells based on FS and SS, cells can also be separated by whether they express a particular protein. In this case, a fluorophore is often used to stain the protein of interest. Fluorophores used for the detection of target proteins emit light when excited by a laser with the corresponding excitation wavelength. These fluorescent stained cells or particles can be detected individually. Forward and side scattered light and fluorescence from stained cells are split into defined wavelengths and channeled by a set of filters and mirrors within the flow cytometer. The fluorescent light is filtered so that each sensor will detect fluorescence only at a specified wavelength. These sensors are called photomultiplier tubes. Fluorescent light is filtered so that each PMT detects a specific wavelength. The PMTs convert the energy of a photon into an electronic signal – a voltage. Various filters are used in the flow cytometer to direct photons of the correct wavelength to each PMT. [39]



### 3 Materials and Methods

All concentration of nanoemulsions (in mM) stated in this thesis is in fact the lipid mixture concentration. There are 60.000-70.000 lipids per nanodroplet in our nanoemulsion. RGD-peptides per nanodroplet are approximately 500-1.000.

#### 3.1 Materials

##### 3.1.1 RGD/RAD conjugated oil-in-water nanoemulsion

The amphiphilic lipids, cholesterol, 1,2-distearoyl-sn-glycero-3-phosphocholine (DSPC) and distearoyl- sn-glycero-3 phosphoethanolamine-N- [maleimide- (polyethylene glycol)-2000] (MAL-PEG-DSPE) were purchased from Avanti Polar Lipids. The lipids were used at a molar ratio of respectively 1:1.85:0.15. The fluorescent phospholipid, 1,2-dipalmitoyl-sn-glycero-3-phosphoethanolamine-N- (lissamine rhodamine B sulfonyl) (Rhodamine-PE) was purchased from Avanti Polar Lipids. Soybean oil was purchased from Sigma Aldrich. The peptides RGD (c[-RGDf(-S-acetylthioacetyl)K-]) and RAD (c[-RADf(-S-acetylthioacetyl)K-]) were purchased from Peptides International. The dialysis equipment utilized was Spectra/Por Float-A-Lyzer G2, 100kDa molecular weight cut-off, from Spectrum Laboratories.

**Table 1:** De-acetylating buffer, pH 7

Chemical	Amount
Hydroxylamine (NH <sub>2</sub> OH)	1.392g
HEPES (buffering agent)	4.76g
Ethylenediaminetetraacetic acid (EDTA)	0.376g
NaOH tablets	4 tablets
Distilled water	To make a total volume of 40ml

Hepes Buffered Saline (HBS) consists of 2.38g/L Hepes and 8g/L NaCl, adjusted to pH 6.7.

### 3.1.2 Antibodies

Anti-Integrin  $\alpha_v\beta_3$  antibody (clone LM609, MAB1976) was purchased from Merck Millipore. This antibody, which is produced in mice, is a monoclonal antibody against integrin  $\alpha_v\beta_3$  and suitable for e.g. Flow cytometry. Clone LM609 block cell attachment of RGD containing ligand, but it does not interact directly with RGD binding site. Instead it appears to be an allosteric inhibitor of integrin  $\alpha_v\beta_3$ , which binds to a conformational epitope resulting from the post-translational association of the  $\alpha_v$  and  $\beta_3$  subunits. [40]

F (ab')<sub>2</sub>-Goat anti-Mouse IgG (H+L) Secondary Antibody, Alexa Fluor® 488 conjugate was purchased from Thermo Fisher Scientific. This antibody is a polyclonal secondary antibody with well-characterized specificity for mouse immunoglobulins. The antibody is conjugated to the fluorescent molecule Alexa Fluor® 488. [41]

### 3.1.3 Cell cultivation

Human umbilical vein endothelial cells (HUVEC) were purchased from Lonza and utilized in experiments at passage 4-7. HUVEC were cultivated in 75cm<sup>2</sup> tissue culture treated flask (TC75) from VWR International. The cells were cultured in Endothelial cell Basal Medium-2 (EGM-2), with added EGM-2, SingleQuots containing: *FBS 10ml, Hydrocortisone 0.2ml, hGFG 2ml, VEGF 0.5ml, R3-IGF-1 0.5ml, Ascorbic acid 0.5ml, hEGF 0.5ml, GA-1000 0.5ml, Heparin 0.5ml*, from Lonza. For the experiments, HUVEC were seeded in 12-well tissue culture plates purchased from Costar, Corning incorporated. 0.25%/0.02% trypsin/EDTA, Phosphate Bovine Serum (PBS), Fetal Bovine Serum (FBS), Bovine Serum Albumin (BSA) were all purchased from Sigma-Aldrich. Sterile microliter pipette tips and plastic pasteur pipettes were purchased from VWR International, while the sterile pipettes of glass were purchased from Corning Incorporated. Centrifuge tubes were ordered from Corning CentriStar and Sigma-Aldrich.

### **3.1.4 Laboratory instruments**

All experiments and handling of HUVEC were performed in a sterile Laminar Air Flow (LAF) bench from Holten (LaminAir) with the use of sterile technique and equipment. HUVEC are classified as a biological hazard level 2 and it is therefore advisable to handle the cells in a sterile environment to prevent the danger of infection. The cells were cultivated and stored inside the Binder CO<sub>2</sub>-incubator. Heating of growth medium etc. was done in a water bath from Heto (DT Hetotherm). Centrifuging of cells was performed in Megafuge 1.0 from Heraeus instruments (Tamro Med-lab). The cells were counted using Countess™ automated cell counter from Invitrogen. The rolling device Stovall low profile roller from Stovall Life Science Incorporated was used in some experiment to prevent detached cells from sedimentation during incubation. The light microscope from Nikon eclipse TS100, with camera from Andor (Zyla sCMOS) was used to look at and to take picture of the cells.

Flow Cytometer from Beckman Coulter was utilized in analyzing of HUVEC samples, which were exposed to antibodies or nanoemulsions.

## 3.2 Methods

### 3.2.1 Cell cultivation

See section 3.1.3 *Cell cultivation* and 3.2.4.1 *Split and seed*.

### 3.2.2 RGD/RAD conjugated oil-in-water nanoemulsions

Oil-in water nanoemulsions (NE) were synthesized at Nanolab NTNU. The de-acetylation buffer and Hepes Buffered Saline were prepared at Preparation Laboratory at Biophysics, Department of Physics at NTNU.

The lipids cholesterol, DSPC and Mal-PEG-DSPE were directly weighed into small glass jars, and then chloroform was added as solvent to make 3 stock solutions. Calculated amount of each stock solution was mixed. 2.6mg Soyabean oil per  $\mu$ mole lipid mixture and Rhodamine-PE were included in the lipid mixture. 5 $\mu$ l of the freshly prepared de-acetylation buffer was added to an eppendorf tube containing 2.5mg/ml RGD solution and place on a shaking device for 60 minutes. 5ml HBS was added to a pre-weighed 10ml jar and weighed once more, to be able to refill correct amount of distilled water after evaporation. The jar was placed on the magnetic heating device. Dripping of the lipid mixture into the aqueous phase started when the temperature reached 68°C. The lipid mixture was dripped into 5 ml HBS at 70°C under continuously magnetic stirring (1300 rpm). Subsequently, use vortex for a thoroughly mixing. The nanoemulsion was cooled down under tap water and sonicated for 20 minutes in Heat System Ultrasonics, in a water bath to maintain room temperature.

Table 2: Ultra Sonication settings

Time	6 min
Total time	20 min
Temp	Off
Amplitude	17%
Pulse on	0.3 sec
Pulse off	0.7 sec



After de-acetylation, 6  $\mu$ l of activated peptide per  $\mu$ mole of lipid was added to the freshly prepared nanoemulsion and mixed using vortex. The peptide-nanoemulsion mixture conjugated overnight 4°C to react. The nanoemulsions were dialyzed against HBS of pH 7.4 to remove unconjugated RGD and to obtain physiological pH.

The hydrodynamic size and size distribution, and the zeta potential were measured using dynamic light scattering techniques (Malvern, Zetasizer Nano PS). For size measurements 8  $\mu$ l of nanoemulsion suspension was dispersed in 800  $\mu$ l HBS in an ordinary cuvette. Reported values were the average of approximately 50 measurements. The reported values are the means and PDIs after combining the 50 measurements with the Malvern Zetasizer series software. For zeta potential measurements 20  $\mu$ l of nanoemulsion suspension was dispersed in 1.5 ml dH<sub>2</sub>O in a capillary cell (Malvern, DTS1061). Reported values were the average of 300 measurement runs. [42] 1 nanodroplet is around 110 nm in size.

### **3.2.3 Analysis**

#### **3.2.3.1 Analytical instrument**

The fluorescent intensity from the fluorescent dyes Rhodamine-PE and Alexa Fluor®488 was measured utilizing Gallios™ Flow Cytometer from Beckman Coulter. To excite Alexa Fluor 488 goat anti-mouse IgG secondary antibody, a 488nm laser was used. A 561 nm laser was used to excite Rhodamine-PE.

Histogram of the autofluorescent (blank) sample was used to position the fluorescence peak in the center of the first decade on the logarithmic scaled x-axis in the plot in Gallios software. The histogram was positioned by adjusting the gain of the detector, before recording of data was initiated. For each cell sample, collection of data (positively fluorescent cells) was terminated when 10,000 cells had been counted or data had been collected for 300 seconds (5 minutes). Cell counts ranged from 1,000 to 10,000 cells in the experiments.

### **3.2.3.2 Data analysis**

Data from running the cell samples in the Flow cytometer was analyzed using Kaluza® Flow analysis version 1.2 software from Beckman Coulter and was used to determine the percentage of positive fluorescent cells to give the median fluorescent intensity (MFI).

To exclude cellular fragments, debris and agglomerations from the analysis, the cell population was gated in the side scatter versus the forward scatter plot. For the gated cells, a histogram was then created to show the cell count as a function of logarithmic fluorescence intensity. An overlay plot was made and histograms for treated cell samples and the blank sample were included. The overlay marker was set to approximately 3% positive gated cells of the blank sample to exclude autofluorescence.

### **3.2.4 Protocols**

#### **3.2.4.1 Split and seed**

The harvesting of cells was performed by removal of old medium from the cultivation flask, washing with 5ml PBS and detachment using 3ml trypsin for 3-5 minutes at 37°C. After looking in the light microscope to confirm detachment of cells, 10 ml medium was added to stop the trypsinization. 12ml of homogenous cell suspension was transferred to a centrifuge tube and centrifuged at 1500 rpm (rotations per minute) for 5 minutes. While centrifuging, droplets from the remaining amount (1ml) of cell suspension in the flask were transferred onto a cell counting chamber slide and cells were counted using a digital cell counter. After centrifuging, the supernatant was removed and the calculated amount of medium was added to achieve a stock concentration of 300.000 cells/ml. The cell suspension was re-suspended to achieve a homogenous suspension. 1ml (containing 300.000 cells) was transferred into a new flask for continuous cell culturing. For experiments, cell suspension and medium to make the desired concentration of cells was seeded into each well in a 12-well plate. Well plates and flasks containing cells were stored in the incubator measuring a temperature of 37°C and a CO<sub>2</sub> level of 5%. Prior to use, medium, PBS and trypsin were heated in the water bath at 37°C.

### 3.2.4.2 Integrin staining

On the day of seeding, cells were harvested from the cell cultivation flask, following the description in section 3.2.4.1 *Split and seed*. Since we only wanted to examine the expression of  $\alpha_v\beta_3$  integrins, experiments were performed on ice. At 4°C the endocytosis and hence the cellular uptake is inhibited.

On the day of experiment, 1%BSA in PBS was prepared and placed on ice. Suitable sterile equipment was brought inside the LAF bench. The primary antibody solutions were prepared directly prior of the experiment. The well plate with the seeded cells was placed on ice for 2 minutes. After removal of medium, the wells were washed once with 1 ml ice cold 1%BSA in PBS. The cells, except the blank samples and the controls, were incubated on ice for 45 minutes with 300µl of anti-integrin  $\alpha_v\beta_3$  primary antibody of the correct concentration. The blank samples and the controls were incubated with 300µl 1%BSA in PBS. The staining was performed in duplicates, i.e. two samples per condition.

While incubating with the primary antibody, the secondary antibody solution with a concentration of 0.5 µg/100µl in ice cold 1%BSA in PBS was prepared. Trypsin was heated in the water bath at 37 °C. After primary antibody incubation all wells were emptied and washed 3 times with 1 ml of ice cold 1%BSA in PBS. Subsequently the cells, except the blank samples, were incubated on ice for 30 minutes with 300µl of AlexaFluor488 goat anti-mouse IgG secondary antibody at 0.5µg/100µl in ice cold 1%BSA in PBS. The blank samples were incubated with 1%BSA in PBS.

After incubation with secondary antibody, all wells were washed 3 times with 1 ml ice cold 1%BSA in PBS. 200µl of 37 °C trypsin was added to each well for detachment of cells. The well plate was placed at 37 °C for 3-5 minutes. After looking at the cells in the light microscope and determined that nearly all the cells had detached, 200µl of ice cold 15%FBS in PBS was added to stop trypsination. The well plate was placed on ice. The samples were re-suspended and transferred to flow tubes before running the flow cytometer.

## 3.2.5 Antibody staining

### 3.2.5.1 Optimization of integrin staining

The aim of these experiments was to find the concentration of primary antibody that assures saturation binding of  $\alpha_v\beta_3$  integrins and hence the concentration to use in the following integrin staining experiments.

In these optimization experiments, a concentration of 20.000 cells per well was seeded 2 or 3 days prior to the day of experiment. Six different concentrations of anti-integrin  $\alpha_v\beta_3$  primary antibody were used, ranging from 0.005 to 0.5 $\mu$ g/100 $\mu$ l, to make an antibody saturation curve.

### 3.2.5.2 Integrin expression as a function of cell density

Expression of  $\alpha_v\beta_3$ -integrin is up regulated in proliferating endothelial cells *in vitro*, in the lag phase, while non-proliferating endothelial cells express  $\alpha_v\beta_3$  at low levels, as described in section 2.5 In vitro. The purpose of these experiments was to examine if we could detect differences in integrin expression in different cell densities. The integrin staining was used to assess integrin expression as a function of cell density. We wanted to see whether integrins were less expressed in high cell density compared to the low cell density.

Different cell densities, ranging from 5.000 to 100.000 cells per well, were seeded 2 or 3 days before the experiment. A primary antibody concentration of 0.3 $\mu$ g/100 $\mu$ l was utilized.

The staining experiment was repeated, now with 9 *days* between seeding and day of experiment (9-days seeding regime), to see if the trending results of RGD-NE incubation coincided with integrin expression. The purpose of these experiments was to examine the association between uptake of RGD-NE and the expression of  $\alpha_v\beta_3$  integrins, to see if the trends were coinciding.

## 3.2.6 Nanoemulsion incubation

### 3.2.6.1 Protocol - Incubation with RGD/RAD-nanoemulsions

PBS, medium and trypsin were put in the water bath set at 37°C. By looking at the cells in the light microscope, a determination of the % confluence was made. Pictures were captured using Andor (Zyla sCMOS) camera device connected to Nikon light microscope. Pictures were taken to have a visual comparison of % confluence between experiments.

Buckets of ice were prepared. 10/15%FBS in PBS was placed on ice. Suitable sterile equipment was brought inside the LAF bench.

Directly prior to the incubation, the RGD-NE or RAD-NE was retrieved from the refrigerator. Calculated amount of nanoemulsion and 37°C medium were mixed and re-suspended to make the correct concentration.

The cells were incubated with 300µl RGD-NE or RAD-NE for the desired amount of time. The blank samples were incubated with pure growth medium only. The old growth medium was removed directly before incubating the cells. Finally, when incubation process was completed, all wells were emptied and washed three times with 37°C PBS. Detachment of the cells was done by adding 200µl of 37°C trypsin for 3-5 minutes. After looking at the cells in the light microscope and determined the detachment, 200µl of ice cold 10/15% FBS in PBS was added to stop the trypsination. The well plates were placed on ice. The samples were re-suspended and transferred to flow tubes before running the flow cytometer.

The RGD-NE samples were performed in *duplo*, while the RAD-NE samples were done in *mono*. The RAD-NE served as a control, since the RAD-motif does not bind specifically to  $\alpha_v\beta_3$  integrins.

### 3.2.6.2 Cellular uptake and uptake rate of RGD/RAD-NE as a function of cell density

The aim of these studies was to measure cellular uptake and uptake rate of RGD-NE and RAD-NE as a function of cell density.

Two concentrations of cells, 10.000 and 100.000 cells per well, were seeded at varying times. See table 1 for details.

**Table 3:** Overview of the time of seeding. The table also explains which figure (found in section 4 – Results) is related to the varying times of seeding.

---

	Fig 18	Fig 19	Fig 20
Days between seeding and experiment low cell density (10.000)	2	2	2
Days between seeding and experiment high cell density (100.000)	2	4	9

---

These experiments were performed as described in section 3.2.6.1 Protocol - Incubation with RGD/RAD-nanoemulsions, and details concerning these exact experiments are described below:

The utilized concentrations of RGD-NE and RAD-NE were 0.5mM. The different incubation times were 5, 10, 20 and 30 minutes. The stopwatch was set at 30 minutes when incubations of the 30 min-wells were started. After the first 10 minutes had passed, the 20 min-wells were next to be incubated. The same procedure was done for the other time points. The well plates were placed at 37°C directly after each addition of NE containing medium. The utilized concentration of FBS in PBS was 15%.

### 3.2.7 Effect of trypsin on detached HUVEC

The purpose of performing these studies was to examine if trypsin is removing bound but not internalized RGD-NE. The RAD-NE was utilized as a control nanoemulsion.

A split and seed procedure was done as described in *section 3.2.4.1 Split and seed*.

Buckets of ice were prepared and 10%FBS in PBS was placed on ice. After removal of the supernatant, calculated amount of growth medium was added and re suspended to make a concentration of X cells/500µl medium, with X ranging from 50.000 to 100.000 between the repeating experiments.

The cell suspension was transferred into 3 centrifuge tubes; 1 tube for RGD-NE, 1 tube for RAD-NE and 1 tube for pure growth medium. To incubate, the correct amount of RGD-NE and RAD-NE was added to make a final concentration of 0.5mM. The stopwatch was set for 20 minutes and the tubes were placed on top of a rolling device. The blank samples were incubated with medium only. After the initial incubation with nanoemulsions, the cells in the 3 centrifuge tubes were washed by using this procedure: *Centrifuging at 1500 rpm for 3 minutes, removal of supernatant and re-suspending in 5ml 37°C growth medium.* This procedure was repeated once. The stopwatch was set at 60 minutes once the initial centrifuging was done and medium was added to the cells. Subsequently, after the third and final centrifuging, the correct amount of medium was added to achieve the correct concentration of cells in each tube. Samples of 500µl were transferred into 1.8ml cryo tubes. The centrifuge tubes, containing the incubated cells, were immediately placed back on top of the rolling device. The samples transferred to the cryo tubes were centrifuged at 1500 rpm for 2 minutes. The supernatant was removed before 300µl of 10%FBS in PBS was added in half of the samples. In the other half, 150µl of trypsin was added for 3-5 minutes at 37°C. 150µl ice cold 10%FBS in PBS was added after addition of trypsin. The samples were placed on ice until running the flow cytometer. The blank samples were handled and placed on ice at the same time as the samples incubated with nanoemulsions only.

After *60 minutes* of incubation with medium, the cell suspensions in the centrifuge tubes were re-suspended and samples of 500µl were transferred into 1.8ml cryo tubes. The centrifuge tubes were immediately placed back on the rolling device for the remaining 60 minutes incubation. The stopwatch was set at 60 minutes. The samples transferred to the cryo tubes were centrifuged at 1500 rpm for 2 minutes. The supernatant was removed before 300µl of 10%FBS in PBS was added in half of the samples. In the other half, 150µl of trypsin was added and after 3-5 minutes at 37°C, 150µl ice cold 10%FBS in PBS was added stop trypsination. The samples were placed on ice until running the flow cytometer.

After *120 minutes* of incubation with medium, samples of 500 $\mu$ l was taken out of the centrifuge tubes and transferred into 1.8ml cryo tubes. The samples transferred to the cryo tubes were centrifuged at 1500 rpm for 2 minutes. The supernatant was removed before 300 $\mu$ l of 10%FBS in PBS was added in half of the samples. In the other half, 150 $\mu$ l of trypsin was added and after 3-5 minutes at 37°C, 150 $\mu$ l ice cold 10%FBS in PBS was added to stop trypsination. The samples were placed on ice until running the flow cytometer.

Directly prior to the flow cytometer analysis, the samples were re-suspended before transferring to flow tubes.

Experiments only comprising of RGD-NE were performed in *duplo*, while experiments comprising both RGD-NE and RAD-NE were performed in *mono*.

### **3.2.8 Saturation binding**

#### **3.2.8.1 Saturation binding of RGD-NE at 37°C**

We wanted to find out if we could get a more quantitative understanding of the binding between RGD-NE and  $\alpha_v\beta_3$  integrins. As a result, an experimental method for measuring the dissociation constant,  $K_d$ , was investigated. We know that RGD-NE binds specifically to  $\alpha_v\beta_3$  integrins. We also wanted to examine how *well* the RGD-NE binds to  $\alpha_v\beta_3$  integrins. Experiments were performed as described in section *3.2.6.1 Protocol – Incubation with RGD/RAD-nanoemulsions*. Details concerning these experiments in particular are added below:

The concentrations of RGD-NE utilized in the first experiment were 0.001mM, 0.01mM, 0.05mM, 0.1mM and 0.5mM. In the following experiments the concentrations utilized were 0.01mM, 0.05mM, 0.1mM, 0.3mM and 0.5mM. The cells were incubated with the different concentrations of RGD-NE for 1 minute. The concentration of FBS in PBS utilized was 10%.



To analyze the obtained saturation curves and estimate  $K_d$ , the following equations were used:

$$K_d = \frac{[\alpha v \beta 3 \text{ integrin}]_{eq} [RGD - NE]_{eq}}{[\alpha v \beta 3 \text{ integrin} + RGD - NE]_{eq}}$$

The dissociation constant ( $K_d$ ) equals concentration of *free*  $\alpha v \beta 3$  integrin multiplied by concentration of *free* RGD-NE divided by concentration of bound  $\alpha v \beta 3$  integrin and RGD-NE.

$$Y = \frac{RGD - NE}{(K_d + RGD - NE)}$$

To calculate the *fractional binding* (fraction bound RGD-NE +  $\alpha v \beta 3$  integrin divided by maximum binding sites available), MFI values were plotted in Excel, the blank (autofluorescent) samples' MFI subtracted and subsequently the MFI values were normalized to the highest value ( $B_{max}$ ) to have values ranging from 0 to 1, since  $K_d$  is defined as ligand concentration (RGD-NE) at 50% (when  $y=0.5$ ) of maximal binding.

### 3.2.8.2 Saturation binding of RGD/RAD-NE at 4°C

To avoid effects of cellular internalization, we also obtained a saturation-binding curve on ice to inhibit the energy dependent endocytosis.

Experiments were performed as described in section 3.2.6.1 *Protocol – Incubation with RGD/RAD-nanoemulsions*. RAD-NE was included in this experiment and both RGD-NE and RAD-NE were performed in *duplo*. Details concerning these experiments in particular are added below:

The cells were incubated for 10 minutes and the utilized concentrations of nanoemulsions were 0.01, 0.05, 0.1, 0.3 and 0.5mM.

## 4 Results

The presentation and interpretation of results is based on trends we can see from curves made of plotted MFI results in software Microsoft Excel and Matlab. Since there are few repetitions of each experiment, mainly  $n=2$  (1-3), there has not been made a statistical analysis of the median fluorescence intensity results. Within each experiment there were usually  $n=2$ , i.e. they were performed in *duplo* and with small differences between the relative MFI values. One data point represents the average MFI value of two samples MFI. The results are usually presented as one representative graph or several experiments combined into one plot for comparison of data series.

The values of MFI from running the flow cytometer were plotted in Excel, blank (autofluorescent) samples' MFI subtracted and subsequently normalized to the highest value of median fluorescent intensity to give *relative MFI*.

### 4.1 Optimization of integrin staining

Analysis of the MFI values from running the flow cytometer showed a flattening of the saturation curve at the concentration range of anti-integrin  $\alpha_v\beta_3$  at 0.1-0.3 $\mu\text{g}/100\mu\text{l}$ , see figure 14. These findings indicated that  $\alpha_v\beta_3$  integrins are saturated within this concentration range in our experimental set-up. Hence, the concentration of anti-integrin  $\alpha_v\beta_3$  that was utilized in the following experiments was 0.3 $\mu\text{g}/100\mu\text{l}$  to assure saturation binding of the  $\alpha_v\beta_3$  integrins. In figure 14, two repeated antibody saturation experiments are combined in one plot. There are small differences, but the curves show the same trend.

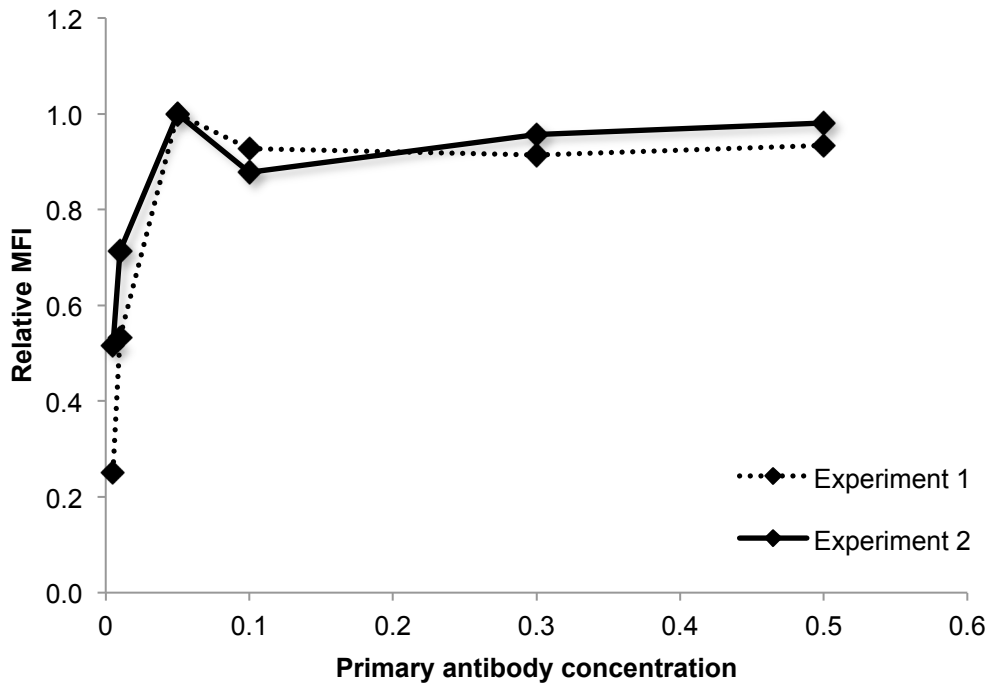


**Figure 14:** Antibody saturation curve. The x-axis gives the relative values of median fluorescent intensity. Each data point represent the average value of two samples' MFI with subtracted blank samples' MFI and subsequently normalized to the highest MFI value to give relative MFI. Here are two repeated staining experiments combined into one plot.

## 4.2 Integrin expression as a function of cell density

Relative integrin expression as a function of cell density was measured using flow cytometry on cell stained for integrin (primary anti-integrin  $\alpha_v\beta_3$  at  $0.3\mu\text{g}/100\mu\text{l}$ ). The confluence of HUVEC on the day of experiment ranged from 30% for the lowest confluent wells and up to approximately 100% for the highly confluent wells. The seeding of HUVEC at cell concentration range of 5.000 – 100.000 cells/ml was done 2 days prior to the experiments.

The results from these experiments showed a 20-30% decrease in integrin expression from the low cell density to the high cell density. In figure 15 the curve shows no decrease of integrin expression from the lowest confluence to the 75% confluence. From 75% to 100% confluence there is a 25% decrease and the total decrease from low to high cell density is 20%. Figure 16 is showing a gradually decrease in MFI from low to high cell density. The histograms in figure 17 show a 27% difference in MFI when comparing low to high cell density. Figure 17

shows results of MFI when utilizing the 9-days seeding regime on high cell density HUVEC. See more details about the different seeding regimes in section 4.3.

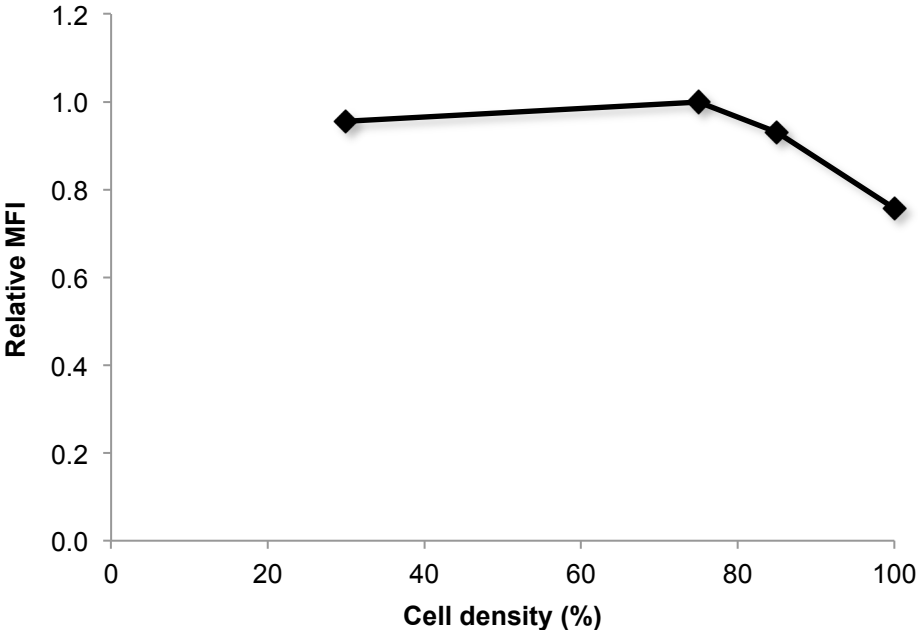


**Figure 15:** Relative integrin expression as a function of cell density as measured with flow cytometry. The curve shows a 20% decrease in MFI from low to high cell density. Seeding of different cell densities of HUVEC was done 2 days prior to experiments.

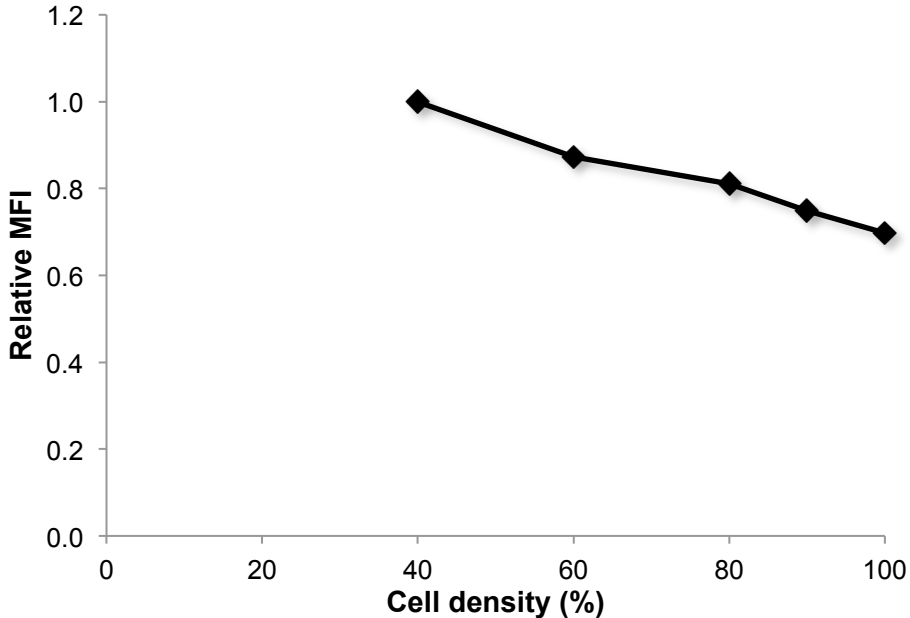
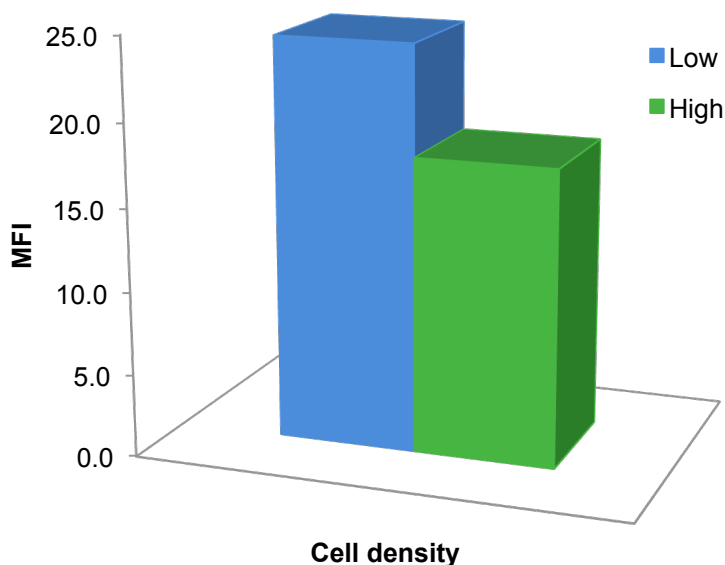


**Figure 16:** Relative integrin expression as a function of cell density as measured with flow cytometry. The curve shows a 30% decrease in MFI from low to high cell density. Seeding of different cell densities of HUVEC was done 2 days prior to experiments.



**Figur 17:** Integrin expression as a function of cell density as measured with flow cytometry. The histograms show 27% decrease when comparing low to high cell density. Seeding of high cell density HUVEC was done 9 days prior to experiments, while low cell density was seeded 2 days before the experiments.

### 4.3 Cellular uptake of RGD/RAD-NE as a function of cell density

The wells with the seeded 10.000 cells (low-density HUVEC) were approximately 75% confluent 2 days after seeding, while the wells containing the seeded 100.000 cells (high-density HUVEC) covered the flask almost 100% after 2 days. Figure 18 shows plotted relative MFI for low and high cell density seeded 2 days prior to experiment.

In one experiment we seeded high-density HUVEC 4 days prior to the day of experiment (and low-density HUVEC was seeded 2 days before the experiment, as usual), see figure 19. Cellular uptake of RGD-NE was measured to have a greater difference between low and high cell density at seeding 4 days before experiment as compared to seeding 2 days before the experiment, see figure 18 and 19. Since the curves seemed to move together after 30 minutes of incubation with nanoemulsion, referred to figure 19, it was decided to try an even extended time between seeding and experiment of the high cell density. In figure 20 the results from the most extensive time between seeding and experiment shows a distinct difference in cellular uptake rate of RGD-NE, from low to high cell density. To achieve cells of distinct difference of low and high confluence on the day of experiment, the optimal time for seeding according

to these studies seemed to be 100.000 cells per well 9 days before and 10.000 cells per well 2 days prior the day of experiment.

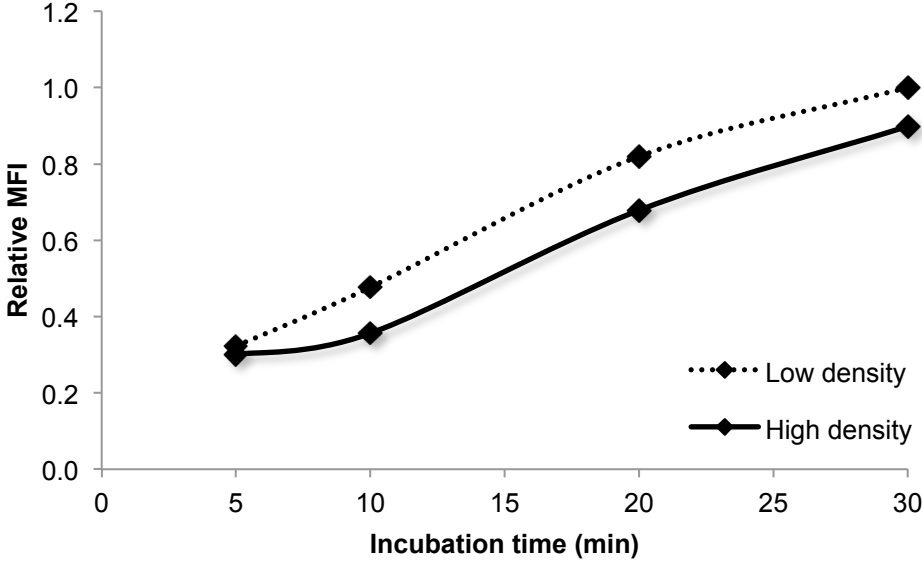


**Figure 18:** Binding and cellular uptake of RGD conjugated nanoemulsion, RGD-NE. The data show cellular uptake of RGD-NE as a function of incubation time. It is a comparison of RGD-NE binding of low versus high cell density with increasing incubation time. Seeding of high cell density and low cell density was done 2 days before the day of experiment.

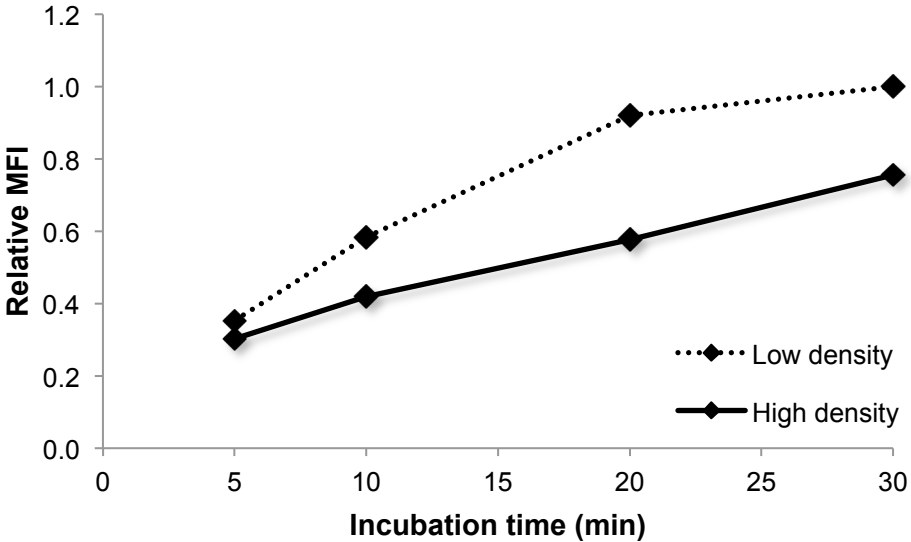


**Figure 19:** Binding and cellular uptake of RGD conjugated nanoemulsion, RGD-NE. The data show cellular uptake of RGD-NE as a function of incubation time. It is a comparison of RGD-NE binding of low versus high cell density, with increasing incubation time. Seeding of high cell density and low cell density was done respectively 4 and 2 days before the day of experiment.

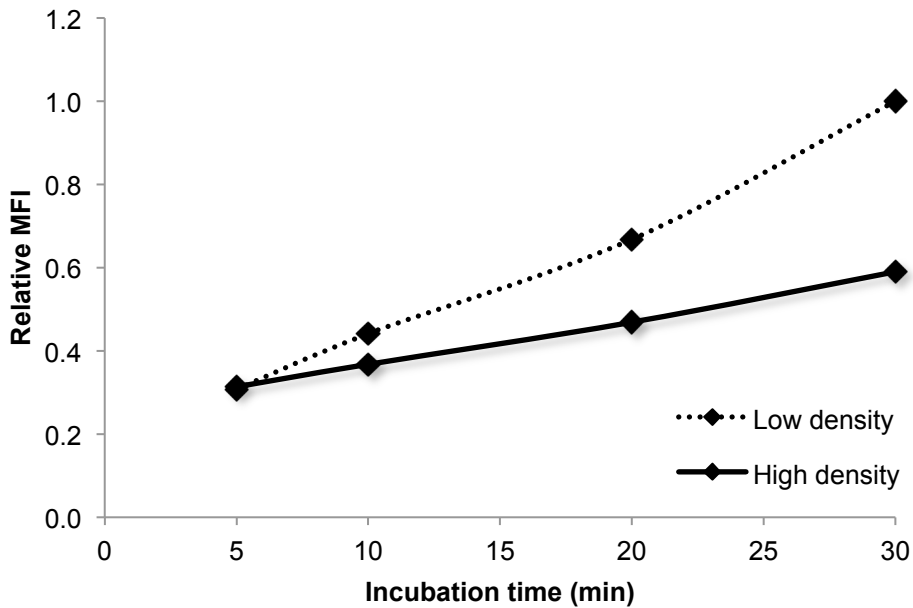
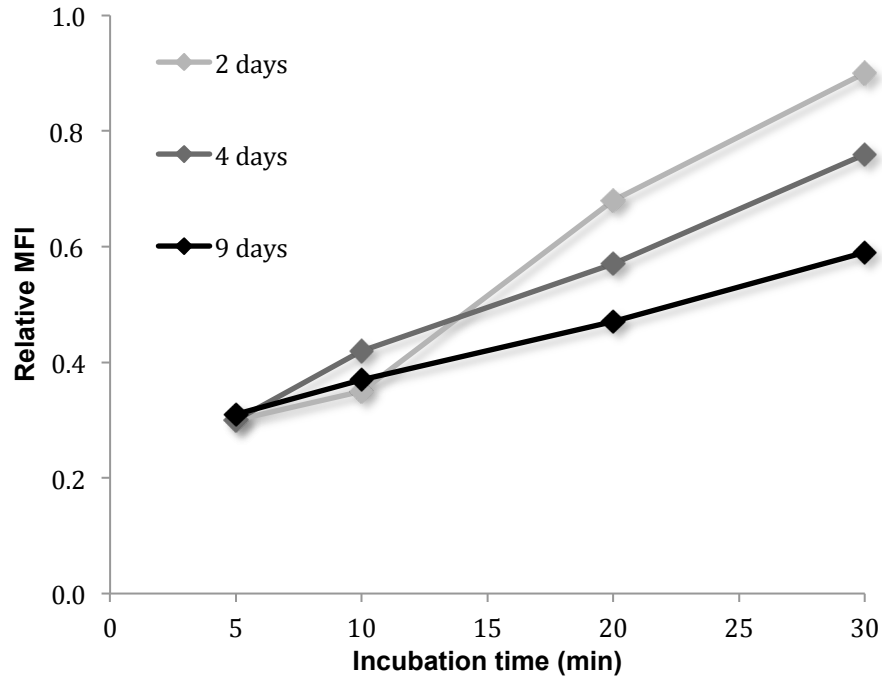


**Figure 20:** Binding and cellular uptake of RGD conjugated nanoemulsion, RGD-NE. The data show cellular uptake of RGD-NE as a function of incubation time. It is a comparison of RGD-NE binding of low versus high cell density with increasing incubation time. Seeding of high cell density and low cell density was done respectively 9 and 2 days before the day of experiment.

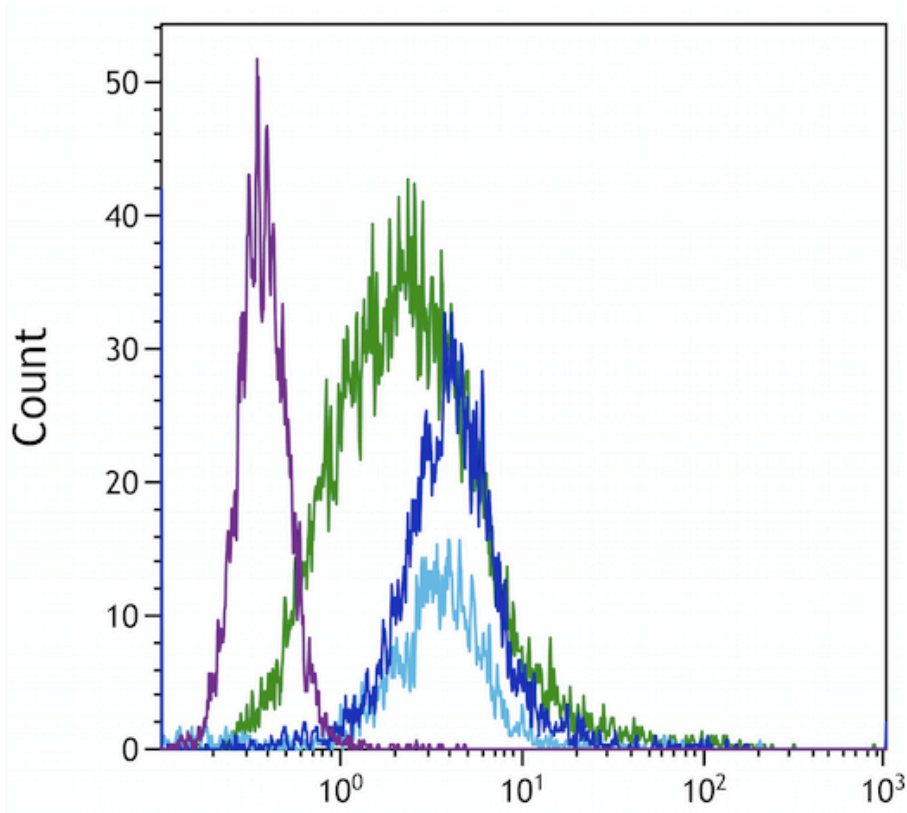
To directly compare results from 2, 4 and 9-days seeding regime for high cell density HUVEC, the relative MFI results of the three different regimes are combined into one plot, see figure 21. The comparison plot indicates distinct differences in relative MFI, illustrated by an increasing flattening with increasing days between seeding and day of experiment.

Figure 22 shows flow histograms of MFI for HUVEC incubated with RGD-NE at 30 minutes. Samples of 2-days and 4-days MFI values are merged into one peak to minimize the difference in cell count between the seeding regimes. The flow histograms show the shifts in x-median with decreasing time between seeding and experiment.

When you compare figure 21 and 22 there seem to be more regular shifts between the three seeding regimes when looking at the curves in figure 21 than illustrated in the histograms in figure 22. There is a clear difference between 2-days and 9-days in both figures.

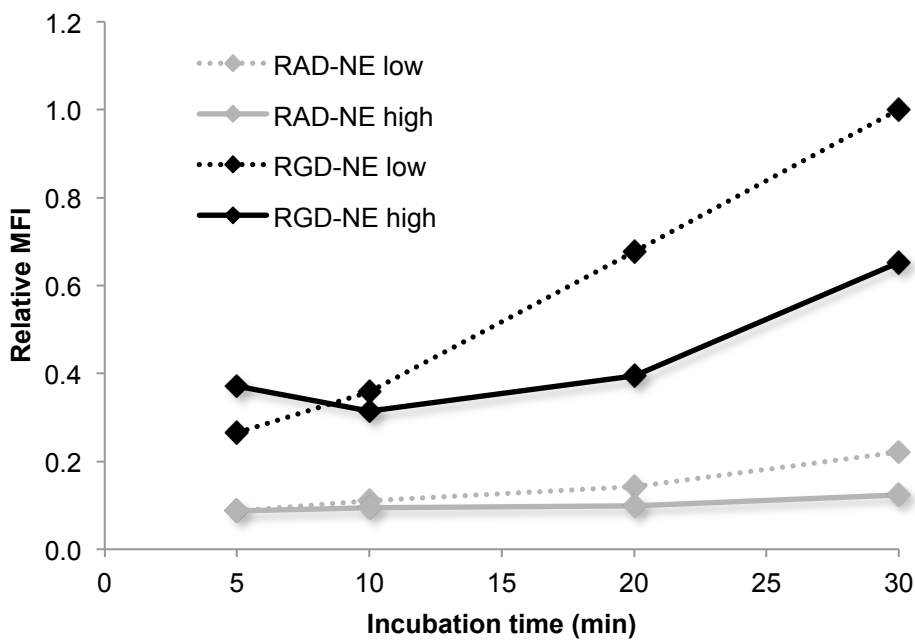


**Figure 21:** Binding and cellular uptake of RGD conjugated nanoemulsion, RGD-NE. The high cell density data of 2, 4 and 9-days seeding (see figure 18, 19 and 20) are here combined into one plot to directly compare the three different seeding regimes. The results are plotted as relative MFI.



**Figure 22:** Binding and cellular uptake of RGD conjugated nanoemulsion, RGD-NE. This plot gives a comparison of the 3 different seeding regimes. **Purple:** blank (MFI=0.37), **green:** 9 days (MFI=2.28), **light blue:** 4 days (MFI=3.42), **dark blue:** 2 days (MFI=4.02). Histograms show fluorescence intensity of samples RGD-NE incubated for 30 minutes. X-axis: fluorescence, y-axis: cell count.

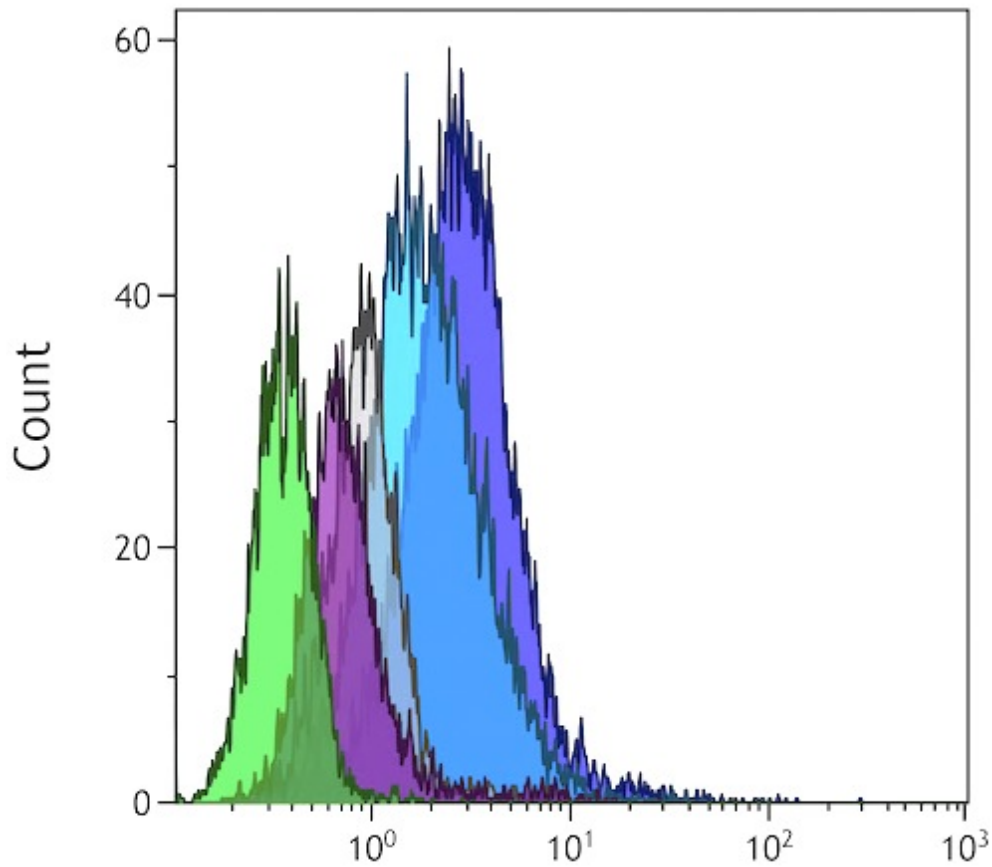




**Figure 23:** Binding and cellular uptake of nanoemulsions, RGD-NE and RAD-NE (control nanoemulsion). HUVEC were incubated with nanoemulsions for 5, 10, 20 or 30 minutes. The figure shows cellular uptake rate of RGD-NE and RAD-NE as a function of cell density. High density HUVEC was seeded 9 days prior to the experiment, while cells of low density was seeded 2 days before the day of experiment.






The experiment performed 9 days after seeding of high cell density, *100.000 cells per well*, showed a clear difference between high and low cell density. The low cell density, *10.000 cells per well* was seeded 2 days before performing the experiment. Due to the interesting findings, this experiment was repeated and the control nanoemulsion, *RAD-NE* was included, see figure 23. The curve plotted for RGD-NE incubation on low cell density HUVEC has an approximately linear shape, and illustrates a 74% increase in relative MFI from 5 to 30 minutes of incubation. The RGD-NE incubation on high cell density shows an almost flat curve from 5 to 20 minutes and then increases 40% from 20-30 minutes of incubation. The total increase of relative MFI for RGD-NE incubation on high cell density HUVEC, when comparing 5 minutes to 30 minutes, is 28%. Despite the increase, there is still a clear difference between low and high cell density at 30 minutes incubation. Incubation of RAD-NE shows little cellular uptake compared to RGD-NE and the trend curve is approximately flat. RAD-NE incubated on low cell density is showing a small increase of 10% in relative MFI at 30 minutes. To illustrate the shifts in MFI at one time point (20 minutes) for the plotted values in figure 23, see flow histograms in figure 24. Table 3 gives the values illustrated in the flow histograms. The difference in x-median MFI between RAD-NE incubated on low and high cell density HUVEC is  $0.92-0.69=0.23$ . RGD-NE incubation on

HUVEC gives a difference in x-median of  $2.84 - 1.80 = 1.04$  MFI when comparing low to high cell density.



**Figure 24:** Binding and cellular uptake of nanoemulsions, RGD-NE and RAD-NE (control nanoemulsion). The overlay diagram illustrates the shifts in median fluorescent intensity for RGD-NE and RAD-NE at 20 minutes of incubation. A blank, *auto fluorescent*, sample is included in the plot to set the background fluorescence of the flow cytometer. The blank sample's MFI, as shown here, is normally within the first decade (0 to 10<sup>0</sup>). X-axis: fluorescence, y-axis: cell count. **Green:** Blank (medium), **purple:** RAD-NE high, **grey:** RAD-NE low, **light blue:** RGD-NE high and **blue:** RGD-NE low. See MFI values in table 3.

**Table 3:** Values and information coincide with flow histograms in figure 24.

Incubated with	Cell density	X-median
 Medium	Low	0.36
 RAD-NE	High	0.69
 RAD-NE	Low	0.92
 RGD-NE	High	1.80
 RGD-NE	Low	2.84

#### 4.4 Effect of trypsin on detached HUVEC

To investigate if Trypsin is removing bound but not internalized nanoemulsion, an experiment on detached cells were performed. The analyzed results indicates a very small difference when comparing uptake of nanoemulsions to uptake of nanoemulsions + Trypsin, see figure 25 below.

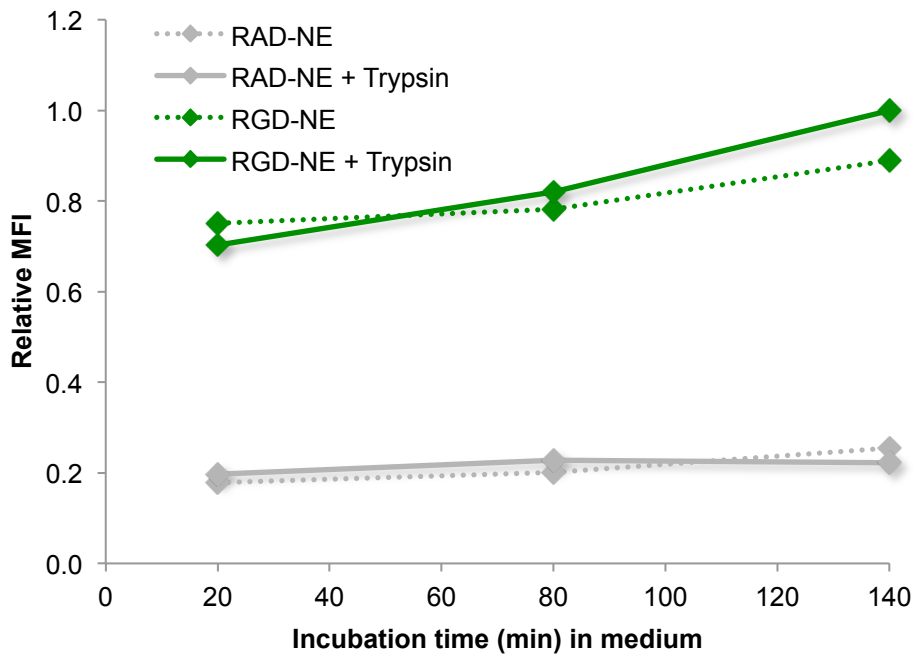


**Figure 25:** Incubation with RGD-NE or RAD-NE on detached cells. After 20 minutes initial incubation with nanoemulsions, the cells were incubated with medium for 0, 60 or 120 minutes (20, 80 and 140 minutes on the x-axis). In half of the samples Trypsin was added for 3-5 minutes at 37°C before adding 10%FBS in PBS. In the other half, 10%FBS in PBS was added after finishing incubation in medium.

The incubation with pure medium was a part of the experiment, to act as a control to which we compare the cells treated with trypsin.

Illustrated in curves in figure 25, the difference between added Trypsin and no Trypsin after incubation seems to be very small. After 2 hours of incubation (20min + 120min = 140minutes) with pure medium after the initial incubation of RGD-NE, the difference is approximately 10% when comparing RGD-NE versus RGD-NE + Trypsin. The results of control nanoemulsion, RAD-NE shows very little cellular uptake. The trend curves are approximately flat and there is practically no difference between RAD-NE and RAD-NE + Trypsin. As the flow histogram illustrates in figure 26, the measured MFI on detached cells with added trypsin versus no trypsin added, are very similar. The flow histograms actually

display small shift to the right of the RGD-NE + Trypsin versus the samples without added Trypsin on detached HUVEC. There is a large difference in MFI values between RGD-NE and RAD-NE, as seen in all other experiments, due to a much higher cellular uptake of RGD-NE.

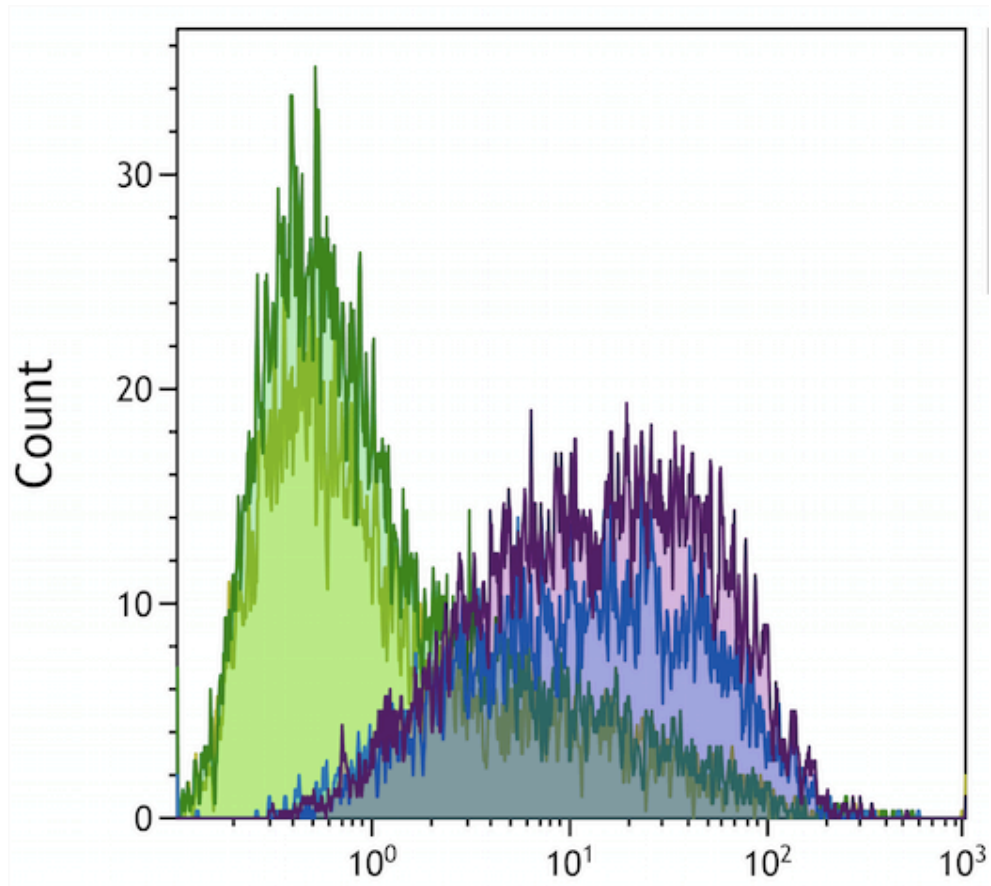


**Figure 26:** Flow histogram showing MFI of incubation with RGD and RAD for 20 minutes on *detached* HUVEC and subsequently 2 hours of incubation in medium. Trypsin was then added in half the samples. In the flow histograms we compare the samples with and without trypsin within each nanoemulsion, RGD-NE and RAD-NE (control). X-axis: fluorescence, y-axis: cell count. **Yellow:** RAD-NE, **Green:** RAD-NE + Trypsin, **Blue:** RGD-NE and **Purple:** RGD-NE + Trypsin. Blank sample is not included in this figure, but was, as in the other experiments, in first decade ( $0-10^0$ ).

#### 4.5 Saturation binding of RGD-NE at 37°C

Data analysis of MFI results in saturation studies was performed using the software Matlab and its *curve-fitting tool*. Fitted saturation curves are displayed in figure 27, *low* cell density, and in figure 29, *high* cell density.

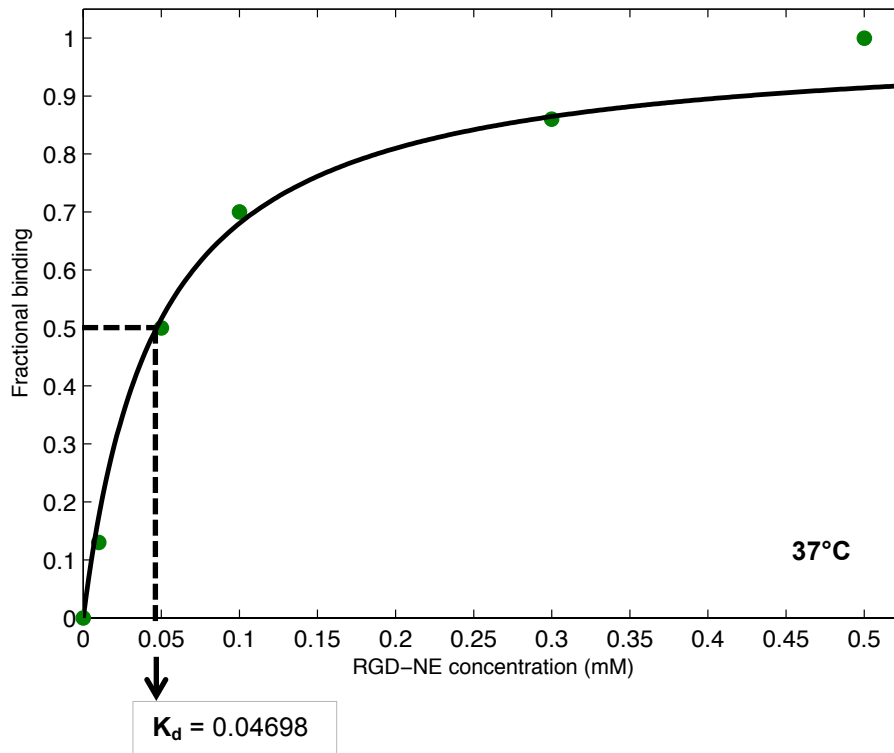


**Figure 27:** Binding and cellular uptake of RGD-NE. The figure shows a fitted saturation binding curve of low cell density HUVEC, incubated at 37°C for 1 minute. The median fluorescent values are normalized to the highest MFI value ( $B_{\max}$ ). The x-axis shows concentration of RGD-NE (mM) and the fractional binding (complex binding divided by maximal available binding sites) along the y-axis.

**Table 4:** Saturation study on low density HUVEC. Values in table 4 relate to figure 27 and figure 28.

Concentration	Median FI	Subtracted blank and normalized to highest
Blank	0.395	0.00
0.01	0.47	0.13
0.05	0.69	0.50
0.1	0.80	0.70
0.3	0.89	0.86
0.5	0.97	1.00

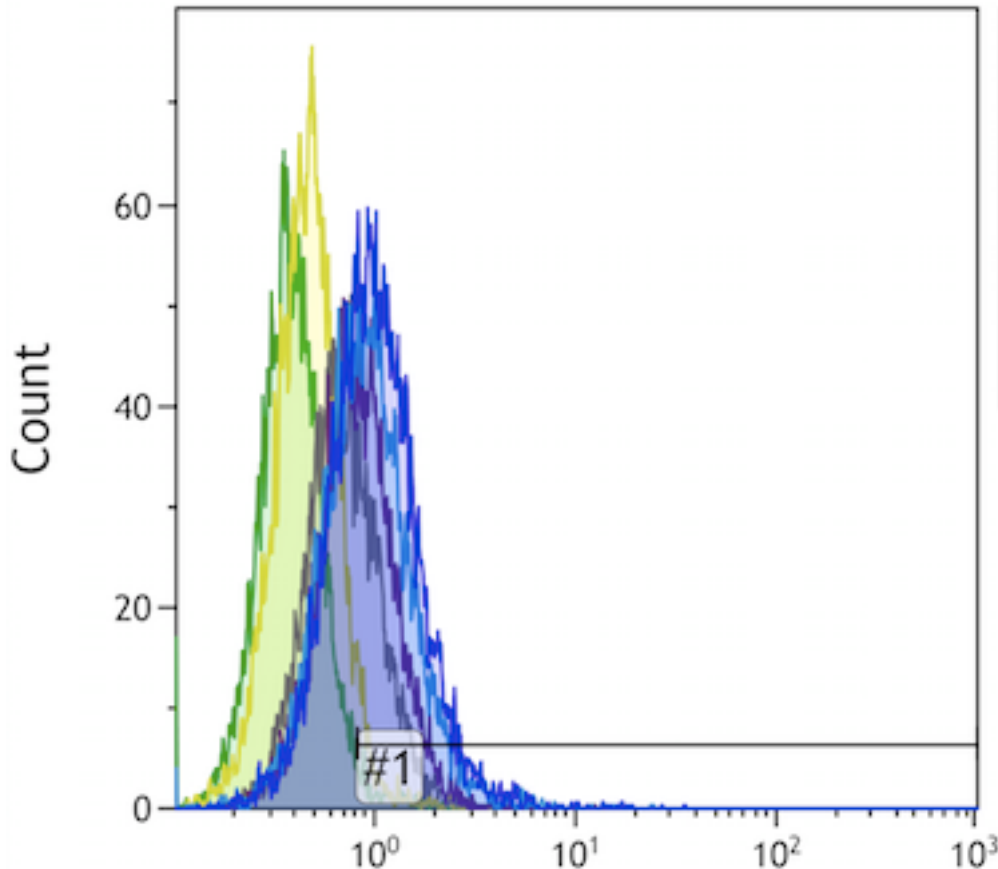


**Figure 28:** Low density HUVEC. All concentrations of RGD-NE are included in this overlay diagram of flow histograms. **Green:** blank sample, **yellow:** 0.01mM, **grey:** 0.05mM, **purple:** 0.1mM, **light blue:** 0.3mM and **blue:** 0.5mM RGD-NE. Here is overlay marker shown, typically set to approximately 3% positive gated cells. MFI values are found in table 5.

As described in section 2.6 *Saturation binding*, we assume that the concentration of the ligand *RGD-NE* at time 0 is a lot higher than the concentration of the receptor  $\alpha_v\beta_3$  integrin at time 0. Therefore we can also state that  $free [RGD-NE] = [RGD-NE]_0$ .

The fitted curve in figure 27 describes the saturation binding kinetics of RGD-NE of one experiment performed on *low* cell density HUVEC incubated at 37°C for 1 minute. The x-axis equals RGD-NE at time 0 for the different concentrations used for incubation. The y-axis represents bound complex of  $\alpha_v\beta_3$  integrin + RGD-NE divided by maximum value,  $B_{max}$ , to give the fractional binding. The dissociation constant,  $K_d$  describes concentration of RGD-NE at half maximal binding [29], The saturation curve increases towards a maximum value,  $B_{max}$ , before a flattening of the curve. The  $B_{max}$  is maximal binding and is given by the maximal binding sites available. The concentration at half maximum binding,  $K_d = 0.04697mM$  for low density HUVEC. The goodness of fit gives a R-square= 0.9874, which indicates a very good fit. The  $K_d$  indicates a good affinity for the complex binding. The curve seems to flatten and

hence saturation occurs around 0.3mM RGD-NE.

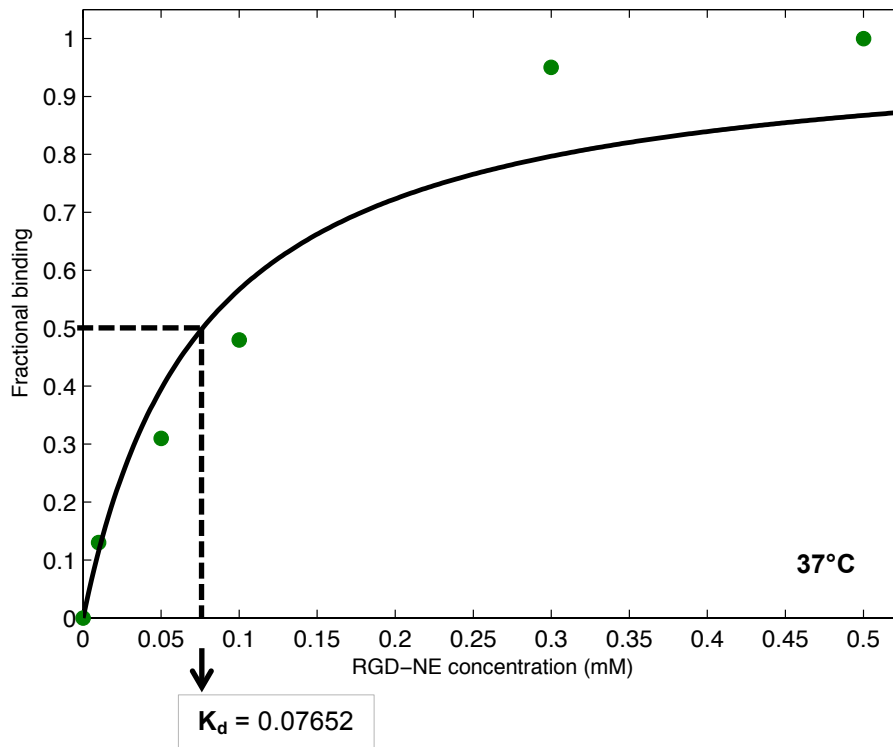


**Figure 29:** Binding and cellular uptake of RGD-NE. The figure shows fitted saturation binding curve of samples from *high* cell density, incubated at 37°C for 1 minute. The x-axis shows concentration of RGD-NE (mM) and y-axis shows measurement of relative median fluorescent intensity: binding of integrin and RGD-NE divided by maximum binding,  $B_{max}$ .

**Table 5:** Saturation studies on high density HUVEC. Values in the table are related to figure 29

Concentration	Median FI	Subtracted blank and normalized to $B_{max}$
Blank	0.385	0.00
0.01	0.51	0.13
0.05	0.70	0.31
0.1	0.87	0.48
0.3	1.33	0.95
0.5	1.38	1.00

In figure 28 the flow histograms illustrates small shift in MFI. The shifts are greater than the shifts in the experiment on 4°C, see figure 31. The fitted curve in figure 29 describes the

saturation binding of RGD-NE on *high* density HUVEC incubated at 37°C for 1 minute. High cell density HUVEC has less expression of  $\alpha_v\beta_3$  integrin than low cell density HUVEC. The concentration at half maximum binding,  $K_d = 0.07654\text{mM}$ . The goodness of fit gives a R-square= 0.9358, which indicates a good fit. The value of  $K_d$  for the high cell density is 1.5 times higher than the  $K_d$  for the low cell density.

#### **4.6 Saturation binding of RGD/RAD-NE at 4°C**

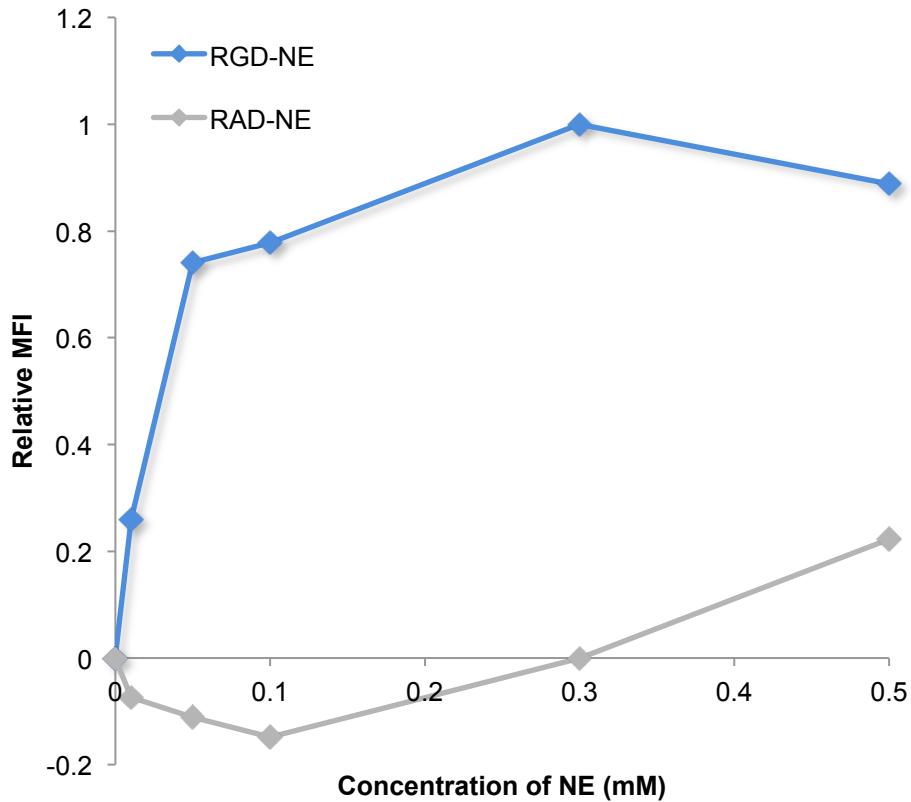
To investigate only binding and no internalization of RGD-NE, the experiment was performed at 4°C. 10 minutes was chosen as a test incubation time as this was probably enough time for binding of RGD-NE to  $\alpha_v\beta_3$  integrin on HUVEC. The control nanoemulsion, RAD-NE was included in this experiment. In figure 30 the plotted results of relative MFI of incubation with RGD-NE show a saturation shaped curve, where integrins seem to be saturated at 0.3mM. The curve of RAD-NE incubation has a different shape and has slightly increased non-specific binding with increasing concentration, as observed for other experiments including control nanoemulsion.

In figure 31 there are presented histograms of measurements in the flow cytometer. The histograms are almost totally overlapping, there are only tiny shift in MFI according to these results.

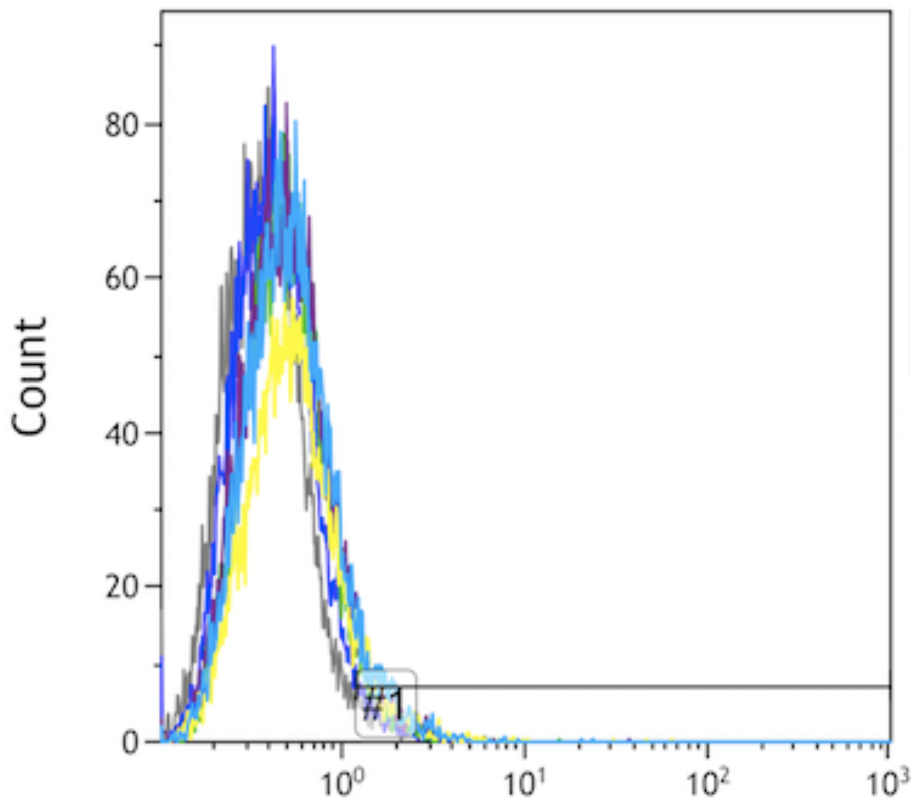
The concentration at half maximum binding,  $K_d = 0.02305\text{mM}$  for low density HUVEC RGD-NE incubated at 4°C, see figure 32. The calculated R-square= 0.98, which indicates a very good fit. The  $K_d$  is lower in the saturation study at 4°C compared to the studies at 37°C (figure 27 and 29). The fact that the  $K_d$  is lower at 4°C indicates a higher affinity for the complex binding than the  $K_d$  values of 37°C studies is showing. RAD-NE shows an approximately flat curve and no typical saturation shape curve.

Figure 33 is included to compare low versus high cell density HUVEC in experiments performed at 37°C. These histograms seem quite similar.





**Figure 30:** Binding of nanoemulsions. The figure shows results of incubation with RGD-NE and RAD-NE at 4°C for 10 minutes.



**Figure 31:** Flow histograms display MFI results of RGD-NE incubation at 4°C. There are tiny shifts in MFI. **Grey:** blank sample, **blue:** 0.01mM, **green:** 0.05mM, **purple:** 0.1mM, **yellow:** 0.3mM and **light blue:** 0.5mM RGD-NE. X-axis: fluorescence, y-axis: cell count. See MFI values in table 6.

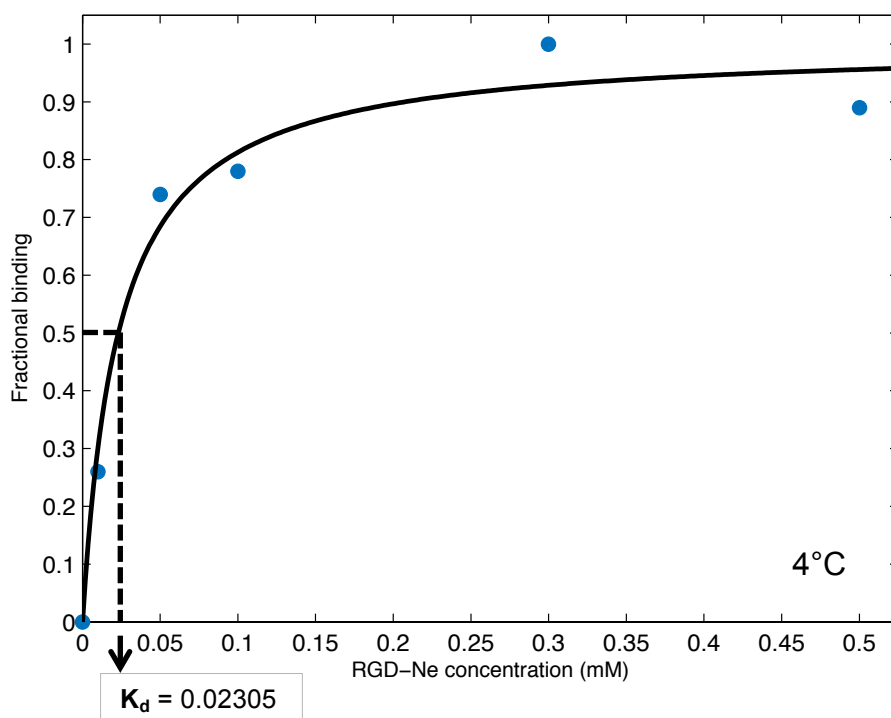


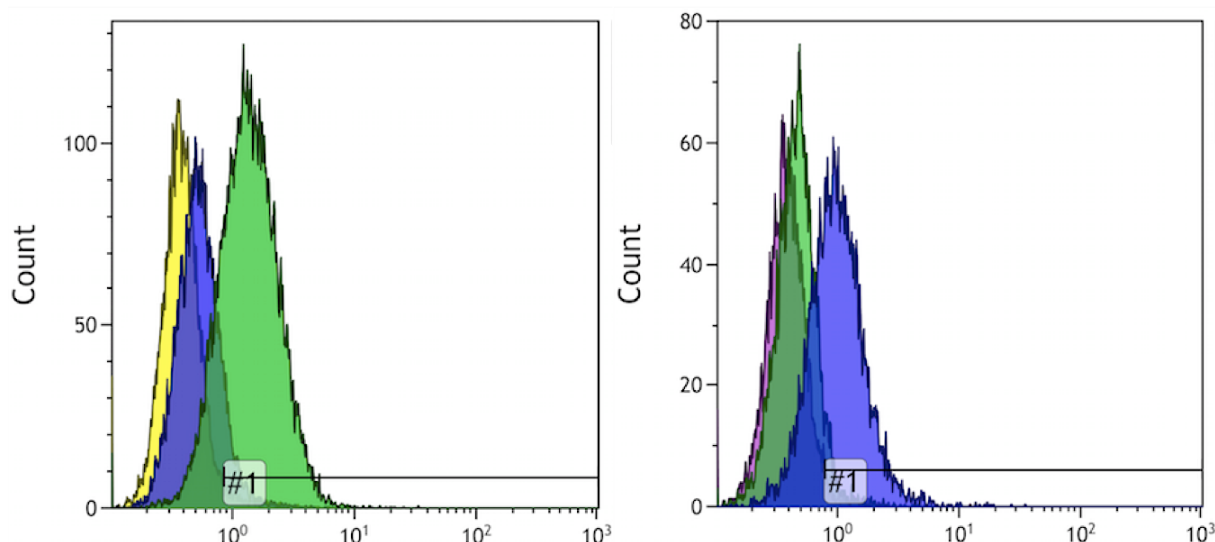
**Figure 32:** Binding of nanoemulsions. The figure shows a fitted saturation curve of RGD-NE incubation at 4°C for 10 minutes.

**Table 6:** Saturation binding at 4°C.

Concentration RGD-NE (mM)	Median FI	Subtracted blank and normalized to $B_{max}$
Blank	0.38	0.00
0.01	0.42	0.26
0.05	0.48	0.74
0.1	0.49	0.78
0.3	0.52	1.00
0.5	0.50	0.89

RAD-NE (mM)	Median FI	Subtracted blank and normalized to $B_{max}$
0.01	0.37	-0.07
0.05	0.37	-0.11
0.1	0.36	-0.15
0.3	0.38	0.00
0.5	0.41	0.22



**Figure 33:** The two overlay display a comparison of low versus high cell density HUVEC when incubating at 37°C. The lowest (0.01mM) and highest (0.5mM) concentration of RGD-NE utilized in the experiments is presented, and the blank sample

#### 4.7 Comparison of $K_d$

In a study performed by Kibria et al., they investigated the effect of liposomal (LP) size on the targeted delivery of doxorubicin to Integrin  $\alpha_v\beta_3$ -expressing tumor endothelial cells. They quantitatively determined the binding constant ( $K_d$ ) for small and large size RGD-PEG-LPs at 4°C and 37°C in HUVEC. The cellular uptake of the RGD-PEG-LPs was measured by incubating HUVEC (40,000 cells/well) in 24-well plate with 500µl of medium consisting of 5, 10, 50, 100, 150 and 200µl of LPs and Krebs's buffer for 2 hours at 37°C. The fluorescence intensity was measured (550nm-590nm). Number of particles was calculated based on the size and the lipid dose of RGD-PEG-LPs. Sigma-plot 12.0 was used to calculate the binding constant ( $K_d$ ) and maximum binding ( $B_{max}$ ) values for small and large size RGD-PEG-LPs.

Table 7: Results from study by Kibria et al.

Sample ID	Binding constant ( $K_d$ value); (no. of particles $\times 10^{10}$ /well)		Binding maximum ( $B_{max}$ ); (maximum fluorescence intensity)	
	4 °C	37 °C	4 °C	37 °C
	Small size PEG-LP	—	—	—
Small size RGD-PEG-LP	2.46 $\pm$ 0.39	6.96 $\pm$ 2.68	79.4 $\pm$ 31.5	223.2 $\pm$ 42.7
Large size PEG-LP	—	—	—	—
Large size RGD-PEG-LP	0.25 $\pm$ 0.11	0.62 $\pm$ 0.52	92.4 $\pm$ 21.1	203.3 $\pm$ 51.8
Relative binding efficiency of	9.70 $\pm$ 2.8	11.2 $\pm$ 6.0	—	—

Compared to small size, large size RGD-PEG-LP showed about a 10 times higher rate of binding and cellular uptake efficiency. This was also tested, by determining the inhibition of cellular uptake of RGD-PEG-LPs, using free RGD. Results presented in table. Binding constant of small size (100nm) RGD-PEG-LP at 4°C, calculated in number of particles is **2.46 \*10<sup>10</sup>/well**, and **6.96 \*10<sup>10</sup>/well** for small size RGD-PEG-LP at 37°C.

The calculated K<sub>d</sub> at 4°C in our experiments was 0.02305mM and 0.04698mM at 37°C (low density). Conversion to number of particles:

$$(K_d) C = 0.02305\text{mM} = 0.02305 * 10^{-3} \text{ M}$$

$$V = 300\mu\text{l} = 300 * 10^{-6} \text{ L}$$

$$n = C * V = 0.02305 * 10^{-3} \text{ M} * 300 * 10^{-6} \text{ L} = 6.915 * 10^{-9} \text{ mole}$$

$$\text{No. of amphiphilic lipids} = n * \text{Avogadro's constant} = 6.915 * 10^{-9} \text{ mole} * 6.022 * 10^{23} = \underline{4.15 * 10^{15}}$$

Since concentration of K<sub>d</sub> is stated in concentration of amphiphilic lipids, we have to divide by 70.000 (which is the number of lipids per nanodroplet/particle.) to get the number of nanodroplets/particles:

$$4.15 * 10^{15} / 70.000 = \underline{5.9 * 10^{10}}$$

$$(K_d) C = 0.04698\text{mM} = 0.04698 * 10^{-3} \text{ M}$$

$$V = 300\mu\text{l} = 300 * 10^{-6} \text{ L}$$

$$n = C * V = 0.04698 * 10^{-3} \text{ M} * 300 * 10^{-6} \text{ L} = 14.09 * 10^{-9} \text{ mole}$$

$$\text{No. of amphiphilic lipids} = n * \text{Avogadro's constant} = 14.09 * 10^{-9} \text{ mole} * 6.022 * 10^{23} = \underline{8.49 * 10^{15}}$$

$$\text{No. of nanodroplets/particles: } 8.49 * 10^{15} / 70.000 = \underline{1.2 * 10^{11}}$$

The size of the utilized nanoparticles (NE) in this thesis is approximately 110nm. The small sized LPs in the Kibria study were approximately 100nm. In the saturation binding experiments, as well as in other experiments in this thesis, there have been used 12-well plates for seeding of HUVEC and 20.000 cells/well was the concentration of cells utilized in the saturation studies. The K<sub>d</sub> (indicated in *no. of particles \* 10<sup>10</sup>/well*) value of incubation based on RGD-PEG-LP at 4°C in HUVEC in the Kibria study, was measured and calculated to be

**2.46.** In this thesis, the measured and calculated  $K_d$  (indicated in no.of particles/well) is **5.9**. If only the digits are compared, and no other factors, the values are similar. The  $K_d$  (indicated in no.of particles\* $10^{10}$ /well) At  $37^\circ\text{C}$  incubation of nanoparticles, there is also some similarities in the values:  **$6.96 * 10^{10}$**  for RGD-PEG-LP (Kibria) and  **$1.2 * 10^{11}$**  for RGD-NE (this thesis).

## 5 Discussion

### 5.1 Optimization of integrin staining

The saturation curve started to flatten at concentrations of anti-integrin  $\alpha_v\beta_3$  in the range of 0.1-0.3  $\mu\text{g}/100\mu\text{l}$ , see figure 14 in section 4.1. The decision of utilizing 0.3 $\mu\text{g}/100\mu\text{l}$  in the following experiments with integrin staining was based on the assurance of saturated  $\alpha_v\beta_3$  integrins at that concentration. 0.3 $\mu\text{g}/100\mu\text{l}$  anti-integrin  $\alpha_v\beta_3$  was the correct concentration to utilize to be certain of saturation, but it might have been sufficient to use a slightly lower concentration, e.g. 0.2 $\mu\text{g}/100\mu\text{l}$ .

The shape of the curves after plotting the results were as expected, except from one point. The plotted results for concentration of 0.05 $\mu\text{g}/100\mu\text{l}$  anti-integrin  $\alpha_v\beta_3$  were slightly off a normal shaped saturation curve. This result could be due to coincidence as the fact that we were dealing with very small amounts of antibodies. Small amounts are tricky regarding pipetting e.g., and the percentage error becomes greater the smaller the amounts we are working with. When pipetting it was made certain that there were no air bubbles, as air bubbles would have affected the concentration and hence the result.

### 5.2 Integrin expression as a function of cell density

Experiments performed with antibody staining of  $\alpha_v\beta_3$  integrins showed a 20-30% decrease in MFI from the lowest to the highest cell density, referring to figure 15 and 16 in section 4.2. The latter experiment using the 9-days seeding regime also showed a similar decrease of MFI in percentage, 27%, see figure 17. Based on these findings the integrin expression in HUVEC do not seem to decrease more than approximately 30% within the highly confluent cells, independent of seeding regime. These findings may indicate that the HUVEC have reached their lower integrin levels already at 100% confluence with seeding performed 2-3 days before experiments.

A possible explanation for the equal levels in integrin expression is that not all unbound fluorescent antibody was removed during the washing steps. A control sample only incubated with secondary antibody solution was included in the initial experiments to make sure the washing technique fully remove unbound antibodies, so most likely this is not a source of error. Weekly bound fluorophores might find its way into the cell by passive transport processes and contribute to fluorescence intensity.

Because confluence in percent is based on a subjective estimate given upon a visual check under the light microscope, it could be a source of error. It is difficult to give a precise measurement of the confluence. This source of error will be minimized with increased experience in working with cell culturing. The same person made the visual estimate and therefore the confluence was estimated in the same way each time. This is an advantage that will also contribute to decrease the percentage error of correct confluence.

### **5.3 Cellular uptake rate of RGD-NE as a function of cell density**

The trend curves of plotted MFI results show, in figures 18, 19 and 20 in section 4.3, an increasing difference between low and high cell density with increasing incubation time of RGD nanoemulsion. From these results it seems that the binding and cellular uptake of RGD-NE by HUVEC is decreasing with time between seeding and experiment for the high cell density. 9-days regime shows a more flattened shaped curve than 2- and 4-days regime and thus indicating that increased time between seeding and experiment has an impact on the binding and uptake of RGD-NE on high density HUVEC.

The analyzed results regarding the different seeding regimes shows a distinct difference in cellular uptake of RGD-NE, when comparing the 2-days regime with the 9-days regime. However, the integrin levels are quite similar in these different regimes. These trends may indicate that there are other mechanisms, besides levels of integrins, involved in the binding and uptake of RGD-NE. The similarity in integrin levels could also be due to internalization of stained integrin by energy-*independent* pathways. [43] The obtained results could then be a combination of both intracellular and extracellular integrin and give a false positive result. Flow cytometry is not able to distinguish between surface bound (extracellular) and internalized (intracellular) fluorophores.

If the levels of integrin receptors are the same on fully confluent wells, independent of seeding regime, we can assume other explanations than integrin levels affecting the RGD nanoemulsion binding. Or the level stays the same, but the density (for some how) changes. So the integrin levels in cultured HUVEC decreases until fully confluence, and then remains at the same level.

One explanation of integrin levels not coinciding with RGD-NE internalization could be that the recycling of integrin is affected or altered in some way. Binding complexes of RGD-NE and integrins enter the cell through endocytic pathways. Subsequently after the internalization process, the integrins are normally recycled back to the cell surface, ready for binding of new ligands. If incubation occurred when the *adhesion turnover* provided the cell with a fresh pool of integrins to engage the matrix and generate new adhesions, this could also affect the binding and internalization at that time. [12]

Another explanation for these findings could indicate that *one* RGD-NE needs *several*  $\alpha_v\beta_3$  integrins to have a sufficiently strong binding. If this explanation is correct it might indicate that the distribution of  $\alpha_v\beta_3$  integrins is altered. The receptor density is perhaps altered and this could have impact on ligand binding. *Receptor clustering* is defined as a non-homogenous expression of receptors on the cell surface. [44] Receptor density, *distribution*, and clustering may be key spatial features that influence effective and proper physical and biochemical cellular responses to many regulatory signals. Classical equations describing this kind of binding kinetics assume the distributions of interacting species to be homogeneous, neglecting by doing so the impact of clustering. [44]

The extracellular matrix, ECM is important in regulation of the integrins. The rigidity, *stiffness*, of the ECM is directly affecting the activation of integrins conformational change from inactive to active and vice versa. [11] A possible explanation for the lower uptake of RGD-NE in the 9-days regime could be that the ECM is altered, less rigid, and therefore the activation of the integrins is negatively affected and decreased binding and internalization as a result. The presence and/or composition of ECM in our in vitro model is uncertain and not investigated, though.



In the experiment with the *9-days* regime there was used a different batch of nanoemulsion than in the *2-days* and the *4-days* experiments. This parameter could have an impact on the comparison between the experiments and these *batch-to-batch* variations are a possible source of error. The lipid concentration is challenging to synthesize precisely from batch to batch of nanoemulsions, small variations will occur. The levels of RGD conjugated to the nanodroplets could differ from preparation to preparation. The sonicator will most likely not produce the exact same product from batch to batch, resulting in slightly different size and size distribution. Levels of fluorophores may also slightly differ. When you look at up take rates this parameter is not that significant, though. Nanoemulsions have a shelf life of 3 weeks, which means we cannot be certain of the stability and quality after that time period. In these experiments, with quite some time between seeding and experiment, it was difficult to perform all experiments within only one batch of nanoemulsion. Since there were used different batches of nanoemulsions within these experiments, that should be taken into consideration when interpreting the results. These experiments should probably have been repeated several times, to give these trending curves an even more reliable result. *Batch-to-batch variation* would still be challenging to overcome in this experimental setup. With an improved timing for the performance of experiments and synthesizing of nanoemulsions, it may work though.

Generally the use of different vials of HUVEC can also be a source of error in *in vitro* experiments. For a period of time there were some challenges with low cell count in the experiments, even though the confluence looked the same from experiment to experiment. Since the microscope with camera attached arrived in January 2016, confluence in experiments performed before that has not been captured. Experiments on 2-days and 4-days seeding regime were performed before January 2016.

There was a low cell count in the 2-days and 4-days experiments, with approximately 1000 positively gated cells per sample. The 9-days experiment had a cell count of 4000-10.000 cells per sample. The median fluorescent intensity from analyzing the sample in the flow cytometer would probably not differ distinctly with higher cell count, but it is a parameter to consider. In figure 22 the 2-days and 4-days samples have been merged into one peak to minimize the difference in cell count compared to the 9-days. There are small shifts in MFI, but the trend is quite clear and shows decreasing MFI with increasing days between seeding

and day of experiment. The flow histograms in figure 22 display results for all concentrations utilized and show similar trends.

The results from experiments with binding and cellular uptake of nanoemulsions show a clear difference in binding and cellular uptake of RGD conjugated nanoemulsions compared to the control nanoemulsion, RAD-NE, referred to figure 23. These results confirm several other findings of previous research in this field, e.g. The RAD-peptide sequence does not bind specific to  $\alpha_v\beta_3$  integrins. There is some binding and cellular uptake of RAD-NE with increasing incubation time, but the result is probably due to non-specific binding onto other parts on the cell surface and uptake by pinocytosis.

#### **5.4 Effect of trypsin on detached HUVEC**

The results, described in section 4.4, show small differences between added trypsin versus no added trypsin on detached cells. The curve indicates a slightly higher cellular uptake of RGD-NE when trypsin is added, about 10%. This result is the opposite of what was the expected outcome. Trypsin is an enzyme, which cleaves peptide chains mainly at the carboxyl side of the amino acids lysine or arginine. [45] The assumption is that Trypsin can potentially cleave other protein and peptide chains, and possibly affect the binding of RGD-NE bound to cell surface  $\alpha_v\beta_3$  integrins. Previous research from a master student gave results that indicted that trypsin could have a negative impact on the binding and hence the cellular uptake of RGD-NE. The studies performed in this thesis showed that this is not the case. Importantly, these findings means that flow measurements of cellular uptake contains both bound and internalized RGD-NE.

#### **5.5 Saturation binding of RGD-NE at 37°C**

The plotted results from these experiments show saturation shaped curves. Although the experiments need to be repeated for a more reliable result, the trend in our experimental set-up shows a steeply rising curve toward saturation, before a flattening (figure 27 and 29). Though there are small shift in MFI when looking at the flow histograms from measurements

in Flow cytometry, the shifts are present and display a trend. Saturation seems to occur even in use of incubation time of 1 minute only. Even though there is a clear flattening of the curve, this part of the curve still shows a slight increase. The slight increase may be due to some internalization of RGD-NE and that the integrins becomes available for binding again, referred to section 2.2, which describes integrins as recycling receptors. Incubation time was set to 1 minute only to achieve enough detectable binding, but minimizing internalization of RGD-NE. Since internalization of RGD-NE may occur at 37°C, even at a very short incubation time, it would be preferable to perform future experiments at 4°C to inhibit endocytosis and cellular uptake.

Measured  $K_d$  in these studies is higher and therefore the affinity lower for the RGD-NE bound to high density compared to low density HUVEC in the saturation studied at 37°C. If the measurement of  $K_d$  is correct, one explanation could be the need for RGD-NE to bind to several integrins to have a strong affinity for and binding to the integrins on the cell surface. If a cluster of integrins is needed, and the clustering is affected in high cell density, this could be the reason why the binding and internalization level is lower for the high versus the low cell density.

There are small shifts in the flow histograms (figure 28), but the result coincide with the saturation curve and gives an estimate on saturation binding of RGD-NE on HUVEC, but there is need for further investigation.

## **5.6 Saturation binding of RGD/RAD-NE at 4°C**

In the saturation studies performed at 4°C there is, as in the 37°C, a steeply increasing curve before saturation. The saturation seems to occur at a concentration of 0.3mM RGD-NE. It was assumed that saturation binding of RGD-NE on surface bound integrins would occur within 10 minutes at 4°C, and that is the reason for choosing that incubation time.

Dissociation constant,  $K_d$  is lower in the experiment performed at 4°C than at 37°C. Since no internalization is occurring at 4°C, this result is plausible. Several repetitions of this experiment have to be done to verify the results presented here. As stated, future experiment would preferably be performed at 4°C. Because there are tiny shift in MFI in this experiment,

the experimental set-up has to be further developed and optimized.

Due to tiny shifts in MFI, where almost all histograms are completely overlapping, this result could be interpreted to not be fully reliable. These experiment have to be repeated and perhaps use different incubation time and/or incorporate higher amount of fluorophore in the nanoemulsions.

Compared to the 4°C studies, the experiments performed at 37°C had greater shift in MFI, when comparing figure 28 (37°C) and 31 (4°C) When comparing low versus high density HUVEC (performed at 37°C), the shifts in flow histograms were similar, see figure 33. Although there are somewhat greater shifts in the 37°C studies compared to 4°C studies, it will, as said, be preferable to optimize an experimental set-up at 4°C.

$K_d$  could be used to compare different sizes of nanodroplets in nanoemulsions. In a paper on dissociation constant and liposomes, they are comparing to different sizes of liposomes. The  $K_d$  values will give an illustration of the affinity on size compared to another [46] One could also compare different types of nanoparticles, e.g. nanoemulsions and liposomes.

## **5.7 Comparison of $K_d$ to the Kibria study**

The calculations and comparison made in results, section 4.7, indicates a similar approach to determine the dissociation constant  $K_d$ , as to this thesis approach. Still, there are differences as the incubation time, size of well plate (24 wells versus 12 wells) and different incubation time. The nanoparticles, in this thesis as to Kibria study, have about the same size. The measured and calculated values of  $K_d$  are similar when comparing the Kibria study by this thesis. There are, as said, inequalities between this thesis approach and Kibria study's approach, but the comparison may indicate that this as a good start for an experimental set-up.

It is emphasized that several experiments need to be performed, preferably on ice (4°C), to have a reliable experimental set-up to find out how well RGD-NE binds to target.

## 6 Conclusion

### 6.1 Thesis work

Antibody staining experiments detected that the level of  $\alpha_v\beta_3$  integrins decreases with increasing cell density, providing the possibility to study targeting as a function of expression levels of the target. There is a correlation with increasing time between seeding and experiment (seeding regime) and decreasing cellular uptake of RGD-NE. When comparing 2, versus 4, versus 9 days between seeding of high density HUVEC, the uptake of RGD-NE decreases with increasing number of days from seeding to the day of experiment. These findings related to different *seeding regimes* have to be more thoroughly investigated. The trend is clear, but since there were parameters like low cell count and the use of different batches of nanoemulsions, several experiments has to be done to make a final conclusion.

As expected, the uptake of RGD-NE on  $\alpha_v\beta_3$  integrins is extensively greater than uptake of the control nanoemulsion, RAD-NE. The control emulsion is most likely taken up by non-specific binding interactions with component of the cell membrane.

In an attempt to characterize the binding of the RGD-NE in a more quantitative manner, saturation studies were performed, to make an estimate of the dissociation constant,  $K_d$ , a measure of affinity. Preferably, the saturation binding studies should be performed at 4°C since the energy-dependent endocytosis will be inhibited and hence the result will reflect only bound and not internalized RGD-NE. The experimental set-up has to be developed and optimized for a more reliable and significant result, though.

### 6.2 Future work

For continuous in vitro work it could be interesting to compare free RGD to RGD-conjugated nanoemulsions, so called competitive studies, [47] containing fixed concentration of RGD-NE and increasing concentration of free RGD measured at equilibrium to find the binding constant. [46] This would be a good addition to the more thoroughly study of the  $K_d$ .

To further investigate the correlation of integrin expression and cellular uptake of RGD-NE as a function of cell density, one experiment is to both incubate HUVEC with nanoemulsion (at 37°C) and subsequently stain with antibodies (at 4°C). In Kaluza, Flow cytometry software, there can be created a plot of detector 1 against detector 2. It is important that the two fluorophores has minimal spillover in excitation and emission spectra, to fully separate them.

To investigate extracellular matrix, ECM, in cultured HUVEC, a 3D-angiogenic assay could be utilized for this matter. [48]

## Literature

1. Net, M.; Available from: <http://www.medicinenet.com/script/main/art.asp?articlekey=3480>.
2. Sønstevold, L. 2014.
3. Ventola, C.L., *The nanomedicine revolution: part 1: emerging concepts*. P T, 2012. **37**(9): p. 512-25.
4. Helgesen, E., *Characterization of the Uptake and Trafficking of avb*, in *Department of Physics*. 2011, NTNU.
5. Hanahan, D. and R.A. Weinberg, *Hallmarks of cancer: the next generation*. Cell, 2011. **144**(5): p. 646-74.
6. Hanahan, D. and R.A. Weinberg, *The hallmarks of cancer*. Cell, 2000. **100**(1): p. 57-70.
7. Avraamides, C.J., B. Garmy-Susini, and J.A. Varner, *Integrins in angiogenesis and lymphangiogenesis*. Nat Rev Cancer, 2008. **8**(8): p. 604-17.
8. Bridgewater, R.E., J.C. Norman, and P.T. Caswell, *Integrin trafficking at a glance*. J Cell Sci, 2012. **125**(Pt 16): p. 3695-701.
9. Caswell, P.T. and J.C. Jim C. Norman, *Integrin Trafficking and the Control of Cell Migration*. Traffic, 2006. **7**: p. 14-21.
10. Caswell, P.T., S. Vadrevu, and J.C. Norman, *Integrins: masters and slaves of endocytic transport*. Nature, 2009. **10**.
11. al., R.Z.e., *Cell-Extracellular Matrix Interactions in Cancer*, in R. Zent and A. Pozzi, Editors. 2010.
12. De Franceschi, N., et al., *Integrin traffic - the update*. J Cell Sci, 2015. **128**(5): p. 839-52.
13. Hak, S., *Optimization of oil-in-water nanoemulsions for tumor targeting and molecular dynamic contrast enhanced MRI*. 2013, NTNU.
14. van Rijdt, S.H., T. Bein, and S. Meiners, *Medical nanoparticles for next generation drug delivery to the lungs*. Eur Respir J, 2014. **44**(3): p. 765-74.
15. Parveen, S., R. Misra, and S.K. Sahoo, *Nanoparticles: a boon to drug delivery, therapeutics, diagnostics and imaging*. Nanomedicine, 2012. **8**(2): p. 147-66.
16. Crist, R.M., et al., *Common pitfalls in nanotechnology: lessons learned from NCI's Nanotechnology Characterization Laboratory*. Integr Biol (Camb), 2013. **5**(1): p. 66-73.
17. Hashizume, H., et al., *Openings between defective endothelial cells explain tumor vessel leakiness*. Am J Pathol, 2000. **156**(4): p. 1363-80.
18. Marelli, U.K., et al., *Tumor Targeting via Integrin Ligands*. Front Oncol, 2013. **3**: p. 222.
19. Schiffelers, R.M., et al., *Anti-tumor efficacy of tumor vasculature-targeted liposomal doxorubicin*. J Control Release, 2003. **91**(1-2): p. 115-22.
20. Mehra, N.K., V. Mishra, and N.K. Jain, *Receptor-based targeting of therapeutics*. Ther Deliv, 2013. **4**(3): p. 369-94.
21. Wiewrodt, R., et al., *Size-dependent intracellular immunotargeting of therapeutic cargoes into endothelial cells*. Blood, 2002. **99**(3): p. 912-22.
22. Amoozgar, Z. and Y. Yeo, *Recent advances in stealth coating of nanoparticle drug delivery systems*. Wiley Interdiscip Rev Nanomed Nanobiotechnol, 2012. **4**(2): p. 219-33.

23. Hatakeyama, H., et al., *Development of a novel systemic gene delivery system for cancer therapy with a tumor-specific cleavable PEG-lipid*. *Gene Ther*, 2007. **14**(1): p. 68-77.
24. Aslund, A.K., et al., *Nanoparticle delivery to the brain--By focused ultrasound and self-assembled nanoparticle-stabilized microbubbles*. *J Control Release*, 2015. **220**(Pt A): p. 287-94.
25. Cressman, S.e.a., *Binding and Uptake of RGD-Containing Ligands to Cellular  $\alpha v \beta 3$  Integrins*. Springer Science, 2008.
26. Booth, R. and H. Kim, *Characterization of a microfluidic in vitro model of the blood-brain barrier (muBBB)*. *Lab Chip*, 2012. **12**(10): p. 1784-92.
27. Brooks, P.C., R.A. Clark, and D.A. Cheresh, *Requirement of vascular integrin  $\alpha v \beta 3$  for angiogenesis*. *Science*, 1994. **264**(5158): p. 569-71.
28. Nisato, R.E., et al.,  *$\alpha v \beta 3$  and  $\alpha v \beta 5$  integrin antagonists inhibit angiogenesis in vitro*. *Angiogenesis*, 2003. **6**(2): p. 105-19.
29. Davis, U.S. *Reversible Binding: 1. Equations and Curves*. 2014.
30. Rowland, M. and T.N. Tozer, *Clinical pharmacokinetics and pharmacodynamics: concepts and applications*, D.B. Troy, Editor. 2011, Lippincott Williams & Wilkins. p. 96-100, 446-448.
31. Hegyi, G.e.a., *Introduction to Practical Biochemistry*. 2013: Eötvös Loránd University.
32. Scientific, T.F. *Fluorescent Probes*. 2015; Available from: <https://www.thermofisher.com/no/en/home/life-science/protein-biology/protein-biology-learning-center/protein-biology-resource-library/pierce-protein-methods/fluorescent-probes.html>.
33. Scientific, T.F. *Physical Properties That Define Fluorescence*. 2015; Available from: <https://www.thermofisher.com/no/en/home/life-science/cell-analysis/cell-analysis-learning-center/molecular-probes-school-of-fluorescence/fundamentals-of-fluorescence-microscopy/physical-properties-that-define-fluorescence.html>.
34. Biosciences, B. *Introduction to flow Cytometry: A Learning Guide*. 2000; Available from: <http://www.d.umn.edu/~biomed/flowcytometry/introflowcytometry.pdf>.
35. Prasad, P.N., *Introduction to biophotonics*. John Wiley & Sons, Inc.
36. Cells, A. *All Cells Flow Cytometry Webinar*. 2013; Available from: <http://www.slideshare.net/allcells/allcells-llc-flow-cytometry-101>.
37. Rahman, M., *Introduction to Flow Cytometry*. AbD Serotec.
38. Semrock. Available from: <https://www.semrock.com/flow-cytometry.aspx>.
39. Abcam. *Introduction to flow cytometry*. Available from: [http://docs.abcam.com/pdf/protocols/Introduction to flow cytometry May 10. pdf](http://docs.abcam.com/pdf/protocols/Introduction%20to%20flow%20cytometry%20May%2010.pdf).
40. Corporation, M.M. *MAB1976H | Anti-Integrin  $\alpha v \beta 3$  Antibody, clone LM609, Phycoerythrin conjugated*. 2016;
41. Scientific, T.F. *F(ab')<sub>2</sub>-Goat anti-Mouse IgG (H+L) Secondary Antibody, Alexa Fluor® 488 conjugate*. Available from: <https://www.thermofisher.com/order/genome-database/antibody/Goat-anti-Mouse-IgG-H-L-Secondary-Antibody-Polyclonal/A-11017>.
42. Hak, S., et al., *The effect of nanoparticle polyethylene glycol surface density on ligand-directed tumor targeting studied in vivo by dual modality imaging*. *ACS Nano*, 2012. **6**(6): p. 5648-58.



43. Maniti, O., et al., *Metabolic energy-independent mechanism of internalization for the cell penetrating peptide penetratin*. *Int J Biochem Cell Biol*, 2012. **44**(6): p. 869-75.
44. Care, B.R. and H.A. Soula, *Impact of receptor clustering on ligand binding*. *BMC Syst Biol*, 2011. **5**: p. 48.
45. Corporation, W.B. *Trypsin*. 2015; Available from: <http://www.worthington-biochem.com/try/>.
46. Kibria, G., et al., *The effect of liposomal size on the targeted delivery of doxorubicin to Integrin alphavbeta3-expressing tumor endothelial cells*. *Biomaterials*, 2013. **34**(22): p. 5617-27.
47. Hulme, E.C. and M.A. Trevethick, *Ligand binding assays at equilibrium: validation and interpretation*. *Br J Pharmacol*, 2010. **161**(6): p. 1219-37.
48. PromoCell. *3D-Angiogenesis Assay*. Available from: <http://www.promocell.com/fileadmin/promocell/PDF/C-13022.pdf>.